fire

MDPI

Article

Realistic Large-Eddy Simulation Study of the Atmospheric Boundary Layer During the Mosquito Wildland Fire and Its Control of Smoke Plume Transport

Kiran Bhaganagar [1,*], Ralph A. Kahn [2,3] and Sudheer R. Bhimireddy [4,5]

[1] Laboratory of Turbulence, Sensing and Intelligence Systems, EB 3.04.16, Department of Mechanical Engineering, 1 UTSA Circle, University of Texas, San Antonio, TX 78249, USA
[2] The Laboratory for Atmospheric and Space Physics, University of Colorado Boulder, Boulder, CO 80303, USA; ralph.kahn@lasp.colorado.edu
[3] Senior Scientist Emeritus, Earth Sciences Division, NASA Goddard Space Flights Center, Greenbelt, MD 20771, USA
[4] Cooperative Institute for Research in Environmental Sciences, University of Colorado, Boulder, CO 80309, USA; sudheer.r.bhimireddy@noaa.gov
[5] Global Systems Laboratory, National Oceanic and Atmospheric Administration, Boulder, CO 80305, USA
* Correspondence: kiran.bhaganagar@utsa.edu; Tel.: +1-210-458-6496

Abstract

Large-eddy simulation (LES) within a weather research and forecasting (WRF) model coupled with an active scalar transport equation was used to simulate Atmospheric Boundary Layer conditions during the Mosquito fire, the largest wildland fire in California during September 2022. The simulations were conducted with realistic boundary conditions derived from the National Oceanic and Atmospheric Administration (NOAA) High Resolution Rapid Refresh (HRRR) model, with the aim of better understanding the two-way coupling between the ABL and plume dynamics. The terrain was extremely inhomogeneous, and the topography varied significantly within the numerical domain. Initially, LES of the smoke-free ABL was conducted on nested domains, and detailed ABL data were gathered from 8 to 9 September 2022. LES simulations were validated using four Automated Surface Observing System (ASOS) stations and NOAA meteorological (MET) observations, as well as NOAA met Twin Otter measurements, and the desired accuracy was established. The smoke plume was then released into the ABL at noon on 9 September 2022, and the plume simulations were conducted for a period of one hour following the release. During this period, the ABL transitioned from convective to buoyancy-shear-driven regimes. Late-night and early-morning conditions are influenced by the complex topography and low-level jet, whereas buoyancy and shear control the ABL dynamics during the morning and afternoon hours. The plume vertical transport is influenced by the ABL depth and the size of the vertical turbulence structures during that time, whereas the wind conditions and turbulent kinetic energy within the ABL dictate the horizontal transport scales of the plume. In addition, the results demonstrate that the plume modifies the microclimate along its path.

Keywords: scalar plume dispersion; convective regimes; high-resolution weather research and forecasting—advanced research (WRF-ARW); passive tracers; convective transport; mosquito fire

Check for updates

Academic Editor: Ali Cemal Benim

Received: 11 November 2025
Revised: 9 January 2026
Accepted: 19 January 2026
Published: 30 January 2026

Copyright: © 2026 by the authors. Licensee MDPI, Basel, Switzerland. This article is an open access article distributed under the terms and conditions of the Creative Commons Attribution (CC BY) license.

1. Introduction

Wildland fire behavior—including spread rate, fire intensity, and plume evolution—is tightly regulated by atmospheric processes across multiple scales. Recent synoptic and mesoscale analysis by Murphy and Mass [1] identified characteristic weather patterns associated with the rapid-growth of California wildfires, including strong offshore flow, low-level jet enhancement, anomalously dry boundary layers, and pressure-gradient–driven winds, establishing a meteorological framework that links large-scale forcing to extreme fire spread and rapid plume development. Early observational and modeling studies by Sun et al. [2] demonstrated that near-surface wind speed, boundary-layer stability, and turbulence intensity exert first-order control on fire spread and heat transport. Building on this, Potter [3] emphasized the role of mesoscale meteorological variability in modulating plume rise, smoke dispersion, and fire-induced circulations. Coupled fire-atmosphere simulations by Coen et al. [4] showed that feedbacks between fire heat release and the atmospheric boundary layer fundamentally alter local winds and turbulence, thereby influencing subsequent fire growth. Field and modeling analyses by Clements et al. [5] and Clements et al. [6] further quantify how fire-generated buoyancy enhances entrainment, turbulence production, and pressure-driven inflows near the fire front. More recent synthesis by Heilman [7] highlighted the multiscale coupling between synoptic forcing, boundary-layer structure, and fire-plume dynamics. Observational studies of extreme fire plumes by Lareau [8] revealed the importance of deep convective structures and atmospheric instability in governing plume penetration into the free troposphere. Topography- and convection-driven severity patterns documented by Lecina-Diaz et al. [9] indicate how atmospheric forcing and terrain jointly amplify fire behavior. Furthermore, Dong et al. [10] demonstrated that evolving meteorological conditions strongly modulate fire intensity and plume development, reinforcing the central role of atmosphere-fire coupling in wildfire dynamics. At broader temporal and spatial scales, Abatzoglou et al. [11] demonstrated that anthropogenic climate change has significantly increased the probability of extreme regional fire years globally, effectively preconditioning the atmosphere for more frequent and intense fire-weather-plume coupling. Extending this framework to urban environments, Guirguis et al. [12] identified the compounding roles of extreme downslope winds, anomalous heat, and synoptic-scale pressure gradients in driving the catastrophic 2025 Los Angeles urban firestorm, underscoring how coincident atmospheric extremes can rapidly amplify fire behavior in complex built landscapes.

Within the California Fire Dynamics Experiment (CalFiDE), Carroll et al. [13] conducted coordinated airborne and ground-based observations to directly measure coupled fire-atmosphere dynamics during large western wildfires, including the Mosquito Fire. Using Doppler lidar, in situ thermodynamic measurements, and targeted flight strategies, this work characterized fire-induced inflows, vertical velocity structure, plume buoyancy, and boundary-layer modification in the near-field of active fire plumes, providing process-level insight into plume-ABL interaction and entrainment under strongly forced conditions. Using satellite-based multi-angle remote sensing, Noyes & Kahn [14] analyzed wildfire smoke plumes during the CalFiDE campaign, including the Mosquito Fire, to quantify plume-top heights, vertical injection profiles, and aerosol evolution. Their satellite-based results showed that plume rise and entrainment are strongly controlled by atmospheric stability and wind shear, providing spatially extensive observational constraints on fire-atmosphere coupling and valuable benchmarks for evaluating plume rise representations in coupled fire-atmosphere models. At finer dynamical scales, plume-resolving analysis by Strobach et al. [15] documented the time evolution of a fire-induced plume jet during the Rum Creek Fire, elucidating the mechanisms governing vertical momentum transport, entrainment, and plume-boundary-layer interaction under strongly forced fire-atmosphere coupling. Col-

lectively, this body of work provides compelling evidence that atmospheric conditions and local meteorology exert a dominant control on wildland fire behavior, governing fire spread, intensity, plume evolution, and the strength of fire-atmosphere coupling across scales.

Wildfire plumes actively modify the atmosphere through strong dynamical and thermodynamic feedbacks. Coupled fire-atmosphere modeling studies by Kochanski et al. [16] demonstrated that fire-induced buoyancy can substantially alter near-surface winds and boundary-layer structure in the vicinity of active fires. High-resolution simulations by Menezes et al. [17] further showed that intense heat release generates localized pressure perturbations and fire-induced circulations that reshape the surrounding microclimate. Using large-eddy simulations, Barjeste Vaezi et al. [18] quantified how plume-driven turbulence enhances vertical mixing and modifies thermal stratification within the atmospheric boundary layer. Observational and modeling analyses by Potter and McEvoy [19] revealed that these fire-induced flows can persist beyond the immediate combustion zone, influencing plume rise and downwind transport. Field-based evidence presented by Peace et al. [20] highlighted the role of fire-generated winds and turbulence in sustaining feedbacks between the fire and the ambient flow, while synthesis work by Fromm et al. [21] placed these processes in the broader context of extreme plume development and stratospheric injection.

Collectively, these studies establish a tightly coupled, two-way interaction between wildland fires and the atmospheric boundary layer (ABL), in which plume-induced pressure gradients, buoyant updrafts, and enhanced turbulence feed back onto local winds, stratification, and boundary-layer mixing. Understanding this two-way WF-ABL coupling remains a central and outstanding challenge in atmospheric science. As wildland fires increase in both frequency and intensity under a changing climate [22–24], advancing the fundamental understanding of fire-atmosphere interactions is critical for improving predictive capability, assessing climate impacts, and informing hazard mitigation and adaptation strategies.

It is well established that wildland fires can generate their own weather through intense heat release and buoyancy-driven circulations [25]. A wide range of numerical simulations [4,26–28] and reduced-order or operational fire-behavior models [29] have been developed to predict quantities such as fire spread, plume rise, and transport scales, often emphasizing fire-induced forcing and feedbacks. However, accurately capturing the dynamical interaction between fire plumes and the background atmospheric boundary layer remains a major challenge. Many existing approaches rely on simplified or coarsely resolved representations of the ABL, making it difficult to disentangle the respective roles of ambient boundary-layer structure and fire-induced circulations in controlling plume evolution, particularly for large, plume-dominated fire events.

In regions of complex terrain, the atmospheric boundary layer is further shaped by topographic forcing, which modifies wind profiles, shear layers, turbulence production, and the timing and structure of boundary layer transitions. Sloping terrain, valley-ridge systems, and elevation gradients can induce terrain-driven flows such as jets, slope winds, and localized low-level jets, thereby altering the balance between shear- and buoyancy-driven turbulence. These topographically modulated ABL regimes directly influence plume rise and downstream transport by controlling entrainment efficiency, vertical mixing, and the depth of penetration into the free troposphere. As a result, an accurate representation of wildfire plume dynamics in complex terrain regions requires not only realistic fire forcing but also high-fidelity simulation of the evolving ABL under combined synoptic and terrain-induced influences.

In this context, the present study adopts a foundational approach: We first establish a high-fidelity large-eddy simulation of the evolving atmospheric boundary layer under

realistic synoptic and topographic forcing, explicitly accounting for the influence of complex terrain on boundary layer structure. The ABL is simulated continuously over a 24 h period during the Mosquito Fire, capturing the diurnal evolution of boundary-layer depth, turbulence intensity, terrain-modulated wind shear, and organized vertical motions. By constraining the imposed plume buoyancy using satellite-derived fire radiative power, the fire forcing is physically realistic in magnitude, allowing the analysis to isolate the dominant role of the ambient, terrain-influenced ABL state in governing plume rise, vertical mixing, and horizontal transport.

Wildland fire-atmosphere interaction is inherently multi-parametric, governed not only by the atmospheric boundary layer but also by the nature of the fuel, its spatial distribution, fire size, intensity, and temporal variability. These factors collectively shape fire behavior and plume evolution, and fully resolving their interactions remains a major challenge for coupled fire-atmosphere modeling. While such complexities are not explicitly resolved in the present framework, it is essential to recognize that the ABL represents one of the most difficult yet critically important controlling elements of the system. The depth, stability, turbulence structure, and shear characteristics of the ABL fundamentally constrain plume rise, vertical mixing, and downstream transport, irrespective of the detailed fire configuration. The central contribution of this work is to demonstrate, through detailed large-eddy simulation, that accurate characterization of the evolving ABL regimes under which a wildfire develops is a necessary prerequisite for a physically meaningful interpretation of plume dynamics. By isolating and rigorously quantifying this atmospheric control, the present study provides a foundational step toward an improved understanding of wildfire-ABL coupling and establishes a framework upon which more fully coupled, fuel- and fire-resolved modeling approaches can be built.

Modeling Limitations and Plume Representation

It is well established that wildland fires can generate their own weather through intense heat release and buoyancy-driven circulations [25]. A wide range of numerical simulations [4,26–28] and reduced-order or operational fire-behavior models [29] have been developed to predict quantities such as fire spread, plume rise, and transport scales. However, accurately capturing the dynamical interaction between fire plumes and the background atmospheric boundary layer remains a major challenge, and many existing approaches rely on simplified representations of the underlying physics.

In conventional fire models, the coupling between fire dynamics and atmospheric processes is often weak or absent, particularly for large and intense fire events [26,30,31]. Although coupled fire–atmosphere frameworks such as WRF-Fire [32,33] represent the two-way interactions between fire and flow, they commonly treat smoke and pollutant transport as passive scalars, limiting their ability to represent buoyancy-driven plume dynamics.

Smoke and other pollutants released from wildfires are inherently buoyant, and their atmospheric transport is physically represented as a buoyant plume [34,35]. Upon release into the ABL, plume evolution is governed not only by the magnitude of the fire heat release but also by the thermodynamic and dynamical structure of the ambient flow. In particular, when plumes are released into the convective boundary layer (CBL), their rise, entrainment, and horizontal dispersion are strongly influenced by the competing roles of shear- and buoyancy-driven turbulence [36].

Within the CBL, surface heating generates buoyancy-driven updrafts that organize turbulence into coherent vertical structures, while background wind shear introduces anisotropy and tilting of plume material. The depth of the ABL, the strength and vertical distribution of turbulent kinetic energy, and the structure of the inversion layer together regulate plume penetration and determine whether buoyant material remains confined

within the boundary layer or partially overshoots into the lower free troposphere. Horizontal transport is likewise modulated by the vertical distribution of wind speed and shear, with plume material experiencing rapid advection when embedded in higher-speed flow aloft and slower transport when mixed into the lower ABL.

Accurately capturing these interactions requires resolving the turbulent structures of the ABL at scales comparable to those governing plume entrainment and mixing. Traditional wildfire modeling frameworks often represent smoke as a passive scalar, limiting their ability to capture buoyancy-driven plume dynamics and turbulence production. Recent advances, such as the bPlume–WRF–LES formulation [37–39], address this limitation by treating the plume as an active scalar that dynamically interacts with the atmosphere. This approach explicitly accounts for plume buoyancy and its contribution to turbulence kinetic energy production, enabling a more physically consistent representation of plume–ABL coupling.

The Mosquito Wildland Fire, which began on 6 September 2022, on the western slope of the Sierra Nevada, was California's largest wildfire of the year. The atmospheric conditions before and during the early days of the Mosquito Fire's spread included a combination of a heat wave that produced an all-time high temperature of 116 degrees Fahrenheit (320 K) and vegetation moisture levels close to record lows. On 7 September, the fire grew considerably, developing a massive pyro-cumulus cloud; 8 September was the largest day of growth, as fire activity intensified and became plume-dominated, producing an enormous pyro-cumulonimbus cloud.

The California Fire Dynamics Experiment (CalFiDE) campaign was conducted during August and September 2022 to sample wildfires in northern California and southern Oregon [13]. The field operations were coordinated with the overpasses of NASA Earth Observing System's Terra satellite to obtain regional-scale snapshots of the Mosquito fire plume in the northeast of Sacramento, California, using the space-based Multi-angle Imaging SpectroRadiometer (MISR) instrument [14]. The Mosquito fire was captured by MISR on 8 September around 18.49 UTC. This time corresponds to around 12 p.m. local time in California.

The purpose of this manuscript is two-fold: first, to conduct a multi-domain, 24 h simulation of the ABL in the Mosquito Fire region during 8–9 September 2022 under realistic ambient meteorology; and second, to simulate the release of a fire plume for one hour during this period. The plume is represented as an idealized, steady buoyancy source to isolate the influence of ABL structure on plume transport. This approach represents a controlled experiment rather than a fully coupled fire–atmosphere simulation.

The objectives of this manuscript are as follows:

1. To conduct a detailed fire-event scale large-eddy simulation (LES) of the atmospheric boundary layer over a 24-h period (8–9 September 2022) during the Mosquito Fire, with the goal of characterizing the diurnal evolution of boundary layer depth, turbulence structure, wind shear, and organized vertical motions under realistic synoptic and topographic forcing.
2. To use a high-resolution LES of a buoyant plume, with fire forcing constrained by satellite-derived fire radiative power, as a controlled diagnostic to quantify how the resolved ABL structure governs plume vertical penetration and horizontal transport

The structure of this paper is as follows: Section 2 describes the modeling methodology, the meteorological evaluation is presented in Section 3, detailed ABL analysis is conducted in Section 4, Section 5 examines plume characteristics, and conclusions are presented in Section 6.

2. Methodology

2.1. Numerical Model

Large-eddy simulation within a weather research and forecasting model, coupled with active scalar transport equations, has been developed and validated to simulate buoyant plumes [37,40]. A thorough performance assessment of the WRF-LES model has been conducted to accurately resolve the micro-scale turbulence [37,38,40–42]. For the sake of completeness, the numerical framework is presented briefly here. The governing equations are the compressible Euler equations with eddy viscosity and gravitational forces as follows:

$$\frac{\partial \rho}{\partial t} + \frac{\partial \rho u_i}{\partial x_i} = 0, \tag{1a}$$

$$\frac{\partial \rho u_i}{\partial t} + \frac{\partial \rho u_j u_i}{\partial x_j} = -\frac{\partial p}{\partial x_i} + \frac{\partial \tau_{ij}}{\partial x_j} - \delta_{3i}\rho g, \tag{1b}$$

$$\frac{\partial \rho \theta}{\partial t} + \frac{\partial \rho u_j \theta}{\partial x_j} = \frac{\partial}{\partial x_j}\rho Pr_t^{-1}\mu_t \frac{\partial \theta}{\partial x_j} - \delta_{i3}\frac{h_0 g}{C_p}, \tag{1c}$$

$$\frac{\partial \rho q_m}{\partial t} + \frac{\partial \rho u_j q_m}{\partial x_j} = \frac{\partial}{\partial x_j}\rho Pr_t^{-1}\mu_t \frac{\partial q_m}{\partial x_j} + Q_p, \tag{1d}$$

$$\frac{\partial \rho K}{\partial t} + \frac{\partial \rho u_j K}{\partial x_j} = \mu_t \left(\frac{\partial u_i}{\partial x_j} + \frac{\partial u_j}{\partial x_i}\right)^2 - \mu_t N^2 - \rho \frac{C_k K^{3/2}}{l}, \tag{1e}$$

where ρ is the mixture density, u_i is the velocity component in the i direction, θ is the potential temperature, q_m is the mass fraction of m-th species, and K is the modeled TKE. p is the pressure, τ_{ij} is the modeled stress tensor given by $\tau_{ij} = \mu_t(\partial_j u_i + \partial_i u_j - (2/3)\delta_{ij}\partial_k u_k)$, δ is the Kronecker delta function, C_p is the specific heat capacity at constant pressure, and h_0 is the heat flux applied at the source only. The gravitational term g is considered a body force that acts in the negative vertical direction; Q_p is the flux of the species at the surface.

The eddy viscosity, μ_t, is defined as $\mu_t \equiv C_k l\sqrt{K}$, where $C_k = 0.1$ and l are a length scale given as $l = min[(\Delta x \Delta y \Delta z)^{1/3}; 0.76\sqrt{K}/N]$ if $N > 0$, otherwise $l = (\Delta x \Delta y \Delta z)^{1/3}$, where $\Delta, x\Delta y\Delta z$ are the grid spacing in the x, y, z directions, respectively. Brunt-Väisälä frequency, N, is computed as $N^2 = (g/\theta)\partial_3\theta$.

Pr_t is the turbulent Prandtl number, which is defined as $Pr_t^{-1} = 1 + 2l(\Delta x \Delta y \Delta z)^{-1/3}$. From observations, $Pr_t \gtrsim 0.66$ along the centerline in all plumes.

An ideal gas is assumed in the equation of state; therefore, potential temperature can be related in the equation of state, $p = p_0(\rho R\theta/p_0)^\gamma$, where R is the specific gas constant and γ is the specific heat ratio. In the following discussion, The horizontal and vertical velocities are presented as u_1 and u_3. The spatial directions x_1 and x_3 are replaced by x and z.

Besides the small-scale turbulence modeled in Equation (1e), large-scale quantities, including density, velocities, temperature, and mass fraction, are resolved in the conservation laws Equations (1a)–(1d). Note that density (ρ) is calculated based on the local mass fraction. In addition, the system simulates buoyancy effects without the Boussinesq assumption (i.e., the density is allowed to vary).

Horizontal turbulence and mixing are computed using second-order horizontal diffusion on model levels, whereas vertical mixing is evaluated from the planetary boundary layer (PBL) scheme [41]. The eddy coefficient, K, is computed using the 2-D Smagorinsky first-order closure method [43,44].

2.2. Domain Configuration

The WRF model is configured with three nested domains to conduct the ABL simulations. The physical domain is shown in Figure 1a, and the computational domain is shown in Figure 1b. The topography of the domain is shown in Figure 2. In our previous

studies, we tested and verified the ability of the WRF-LES model to simulate the ABL at scales similar to this study [41,42]. Domains D01 and D02 are nested with feedback turned on and were used for mesoscale simulations. The LES runs were performed in domain D03. The sizes of D01, D02, and D03 are 360 km, 103 km, and 34 km in the horizontal direction, respectively. The horizontal resolutions for the mesoscale domains are 3 km (D01) and 1 km (D02), and for the LES domain, 333.33 m is used for the ABL simulations. For all three domains, the model top is considered at 50 hPa (20 km) with a total of 41 levels, including 12 levels within the ABL. The first grid point is at 24.08 m above the ground. The mesoscale runs are initialized at 00 UTC on 5 September 2022 and run for a period of 4 days. Meteorological initial and boundary conditions for D01 are obtained from datasets provided by the NOAA High-Resolution Rapid Refresh (HRRR) Model. The HRRR is run operationally by the National Centers for Environmental Prediction (NCEP) Environmental modeling center [45] and covers the Continental United States (CONUS) in real-time at a 3-km resolution, is updated hourly, is cloud-resolving, and includes convection. Radar data are assimilated in the HRRR every 15 min over a 1 h period, adding further detail to that provided by the hourly data assimilation from the 13 km radar-enhanced data.

The physics model chosen in WRF is outlined in Table 1.

Table 1. WRF model configuration.

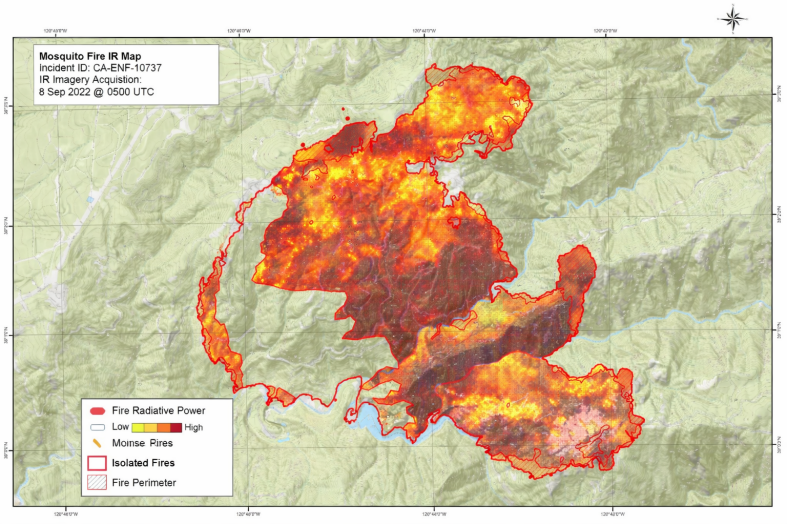
WRF Model Physics	
Longwave Radiation	RRTM scheme [46]
Shortwave Radiation	MM5 scheme [47]
Microphysics	Zhao [48]
Cumulus	Kain-Fritsch [49]
PBL	YSU scheme with ysu_top_downmixing turned “on” [50–52]
Surface layer	Monin-Obukhov [53]
Land Surface model	Noah LSM [54]

2.3. Plume Simulation Configuration and Forcing

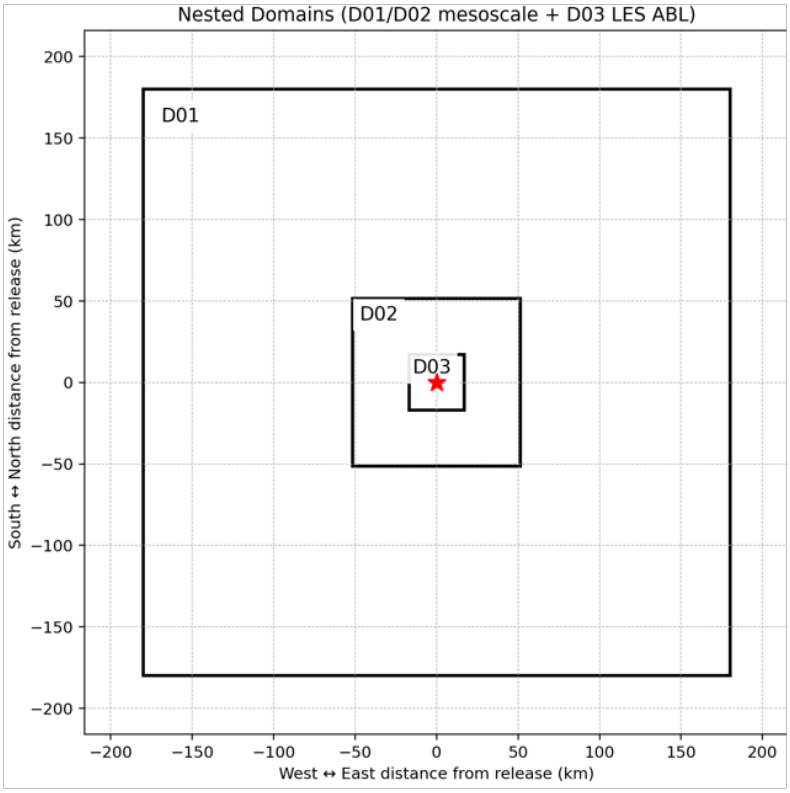
Following the characterization of the ABL evolution, plume simulations are conducted as controlled experiments to isolate the influence of the terrain-modulated ambient ABL on plume transport. At 11 a.m. local time on 9 September 2022, a heated air plume is released into the ABL domain from a continuous circular source located at the ground. The background velocity and temperature profiles, as well as the surface heat flux, are extracted directly from the WRF-LES ABL simulation, ensuring that the plume is introduced into a dynamically consistent atmospheric state representative of the fire-period conditions.

The plume source has a diameter of $D = 400$ m and is centered at (39.006° N, 120.745° W), corresponding to the location of the Mosquito Fire. The source gas is lighter than the ambient atmosphere, and the resulting density contrast generates buoyancy-driven flow. No momentum is imposed at the source; plume motion, therefore, arises solely from buoyancy forcing rather than prescribed inflow velocity.

The large-eddy simulation domain spans 4 km × 4 km × 7 km in the cross-stream, streamwise, and vertical directions, corresponding to $10D \times 10D \times 17.5D$. The plume source is located at the center of the bottom boundary. The domain is discretized using a uniform Cartesian grid with 100 × 100 × 700 grid points in the horizontal and vertical directions, providing adequate resolution to capture plume-scale turbulence and vertical structure.

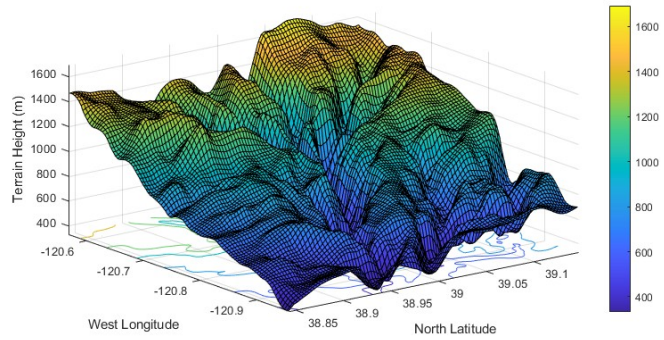


(**a**)

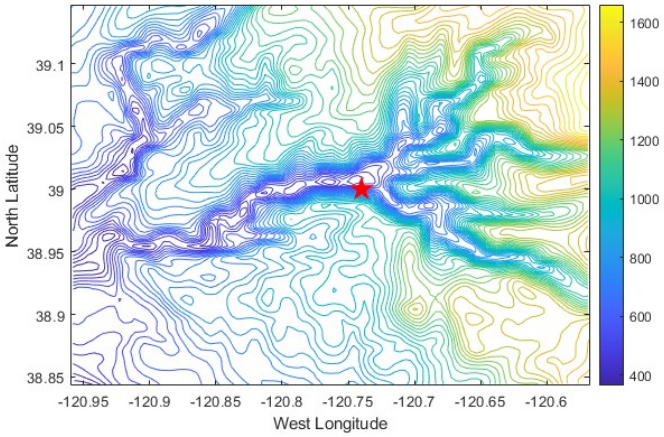


(**b**)

Figure 1. (**a**) Top figure: Location of the mosquito fire. (**b**) Domains (D01, D02, D03) for the WRF-LES simulations. The plume was initialized at 39.006° N, 120.745° W shown as ⋆. The fire area mapped in (**a**) represents an 4 km region centered within the 33 km D03 domain in (**b**). The sizes of nested domains D01, D02 and D03 are 360 km, 103 km and 34 km, in the horizontal direction, respectively. The horizontal resolutions for the mesoscale domains are 3 km (D01) and 1 km (D02), and for the LES domains, 333.33 m is used for the ABL simulations.



(**a**)



(**b**)

Figure 2. The boundary conditions obtained from the HRRR initialization data corresponding to the physical domain D03 used in the LES simulation. (**a**) The height of the terrain vs. latitude-longitude, (**b**) The cross-sectional plane of the terrain. The plume was initialized at the center of the region (39.006° N, 120.745° W).

Periodic boundary conditions are applied at the lateral boundaries, and a constant-pressure boundary condition is imposed at the top of the domain. A constant surface heat flux is prescribed over the plume source region at the bottom boundary, while the remainder of the surface is assigned a zero heat flux. This configuration isolates plume-driven buoyancy forcing from background surface heating unrelated to the fire source.

The source buoyancy flux is defined as $B_0 = 0.25\pi D^2 Q_p g'$ and is prescribed as $B_0 = 1.07 \times 10^4$ m^4 s^{-3}, corresponding to a surface heat flux of approximately 240 W m^{-2}. This value closely matches the MODIS-derived fire radiative power density of ∼230 W m^{-2} reported for the Mosquito Fire by Noyes and Kahn [14], providing an observational constraint on the magnitude of the imposed plume forcing and avoiding arbitrary tuning of source strength.

Plume evolution is simulated for a total duration of 50 min using LES with explicit representation of buoyancy production in the turbulence kinetic energy equation, allowing two-way coupling between the buoyant plume and the ambient ABL. While the plume locally enhances turbulence and vertical transport, the background ABL structure, shaped by synoptic forcing and complex terrain, remains the dominant control on plume rise, entrainment, and downstream dispersion.

Satellite-Derived Fire Radiative Power Background

The fire radiative power estimates used in this study are derived from the Moderate Resolution Imaging Spectroradiometer (MODIS), a spaceborne multispectral imaging instrument aboard NASA's *Terra*[1] and *Aqua* satellites. MODIS provides near-global coverage with multiple overpasses per day and measures radiance in 36 spectral bands spanning the visible to thermal infrared. These capabilities enable the detection and characterization of active fires, land surface temperature, aerosols, and cloud properties.

FRP is retrieved from mid-infrared observations and represents the instantaneous rate of radiative energy release from actively burning fires. It is widely used as a physically based proxy for fire intensity and surface heat release, and has been shown to scale with combustion rate and sensible heat flux in both observational and modeling studies. As such, MODIS FRP provides an independent observational constraint on the magnitude of buoyancy forcing applied in coupled fire–atmosphere simulations.

For the Mosquito Fire period considered here, Noyes and Kahn [14] reports a peak FRP corresponding to an effective surface heat flux of approximately 230 W m^{-2}. This value is used as a reference for the plume forcing magnitude prescribed in the present simulations, as described in Section 2.3.

3. Meteorological Evaluation

The WRF model performance was evaluated against the hourly observations of temperature and relative humidity at 2 m, wind speed, and wind direction at 10 m, collected at four Automated Surface Observing System (ASOS) stations located inside D02 (Figure 3). Surface meteorological observations were obtained from the Automated Surface Observing System, a nationwide network operated by the National Weather Service (NWS), the Federal Aviation Administration (FAA), and the Department of Defense. ASOS stations provide continuous, high-frequency measurements of near-surface atmospheric conditions, including 2-m air temperature, dew point temperature, surface pressure, wind speed and direction at 10 m, precipitation type and accumulation, visibility, cloud base height, and present weather. These observations are quality controlled and reported at temporal resolutions ranging from 1 to 5 min, with standard hourly summaries, making ASOS a primary data source for characterizing boundary-layer conditions relevant to wildfire behavior, plume dispersion, and fire–atmosphere coupling [55].

To compensate for the lack of balloon soundings necessary to perform upper-air model assessments inside D02, the wind profile data collected by the NOAA-MET Twin Otter research aircraft were used. The MET-TO was equipped with Micro-pulse Doppler lidar, which collected the atmospheric backscatter, vertical velocity, and horizontal wind profiles. The MET-TO flew over the fire area several times between 8 September 1800 UTC and 9 September 0000 UTC, and six flight legs of nearly constant altitude were chosen (Figure 4) to compare the WRF simulated wind profiles.

The following metrics: Mean Absolute Error (MAE), Mean Bias Error (MBE), Root-Mean Square Error (RMSE), and Pearson correlation coefficient (R) were calculated to assess the performance of the WRF model against ASOS observations.

[1] MODIS was designed, developed, and manufactured by the National Aeronautics and Space Administration (NASA), Goddard Space Flight Center, Greenbelt, MD, USA, with instrument integration performed for flight aboard the Terra and Aqua satellites.

$$MBE = \frac{1}{n}\sum_{i=1}^{n}(M_i - O_i) \quad (2)$$

$$MAE = \frac{1}{n}\sum_{i=1}^{n}|M_i - O_i| \quad (3)$$

$$RMSE = \sqrt{\frac{1}{n}\sum_{i=1}^{n}(M_i - O_i)^2} \quad (4)$$

$$R = \frac{\sum_{i=1}^{n}(O_i - \overline{O})(M_i - \overline{M})}{\sqrt{\sum_{i=1}^{n}(M_i - \overline{M})^2}\sqrt{\sum_{i=1}^{n}(O_i - \overline{O})^2}} \quad (5)$$

where M_i denotes the model value, O_i is the observed value, and n represents the number of data points.

Surface meteorological fields from the WRF D02 output from 06 September 0000 UTC to 9 September 0000 UTC were used for evaluation. The WRF grid cell corresponding to the ASOS station location was chosen based on the nearest neighbor approach. Performance metrics at individual ASOS stations and averaged across all 4 stations for surface variables are shown in Tables 2 and 3. Overall, the model simulated temperature closely matches the station observations across all 4 sites, with an average mean bias error of 0.02 K. Similar agreement was found with the 2 m relative humidity (RH) and 10 m wind direction fields, with an average bias of 1.36% and 3.35 degrees, respectively. Contrary to the wind direction, the model consistently over-predicted the wind speed at all 4 sites with an average MBE of 1.4 m/s. The wind speeds observed at the ASOS stations were weak to moderate, ranging from 1 to 3 m/s. Given the complex terrain around the ASOS station locations, it is reasonable for the model to deviate from the observed values, especially when the winds are weak to moderate. This somewhat poor performance of the WRF model in simulating the surface winds over complex terrain was observed previously by other researchers ([56,57]). We assessed the sensitivity of the model performance by averaging the model output over 1 to 3 grid cells surrounding the ASOS station locations when comparing it against the observations. However, this did not result in a significant improvement in model performance.

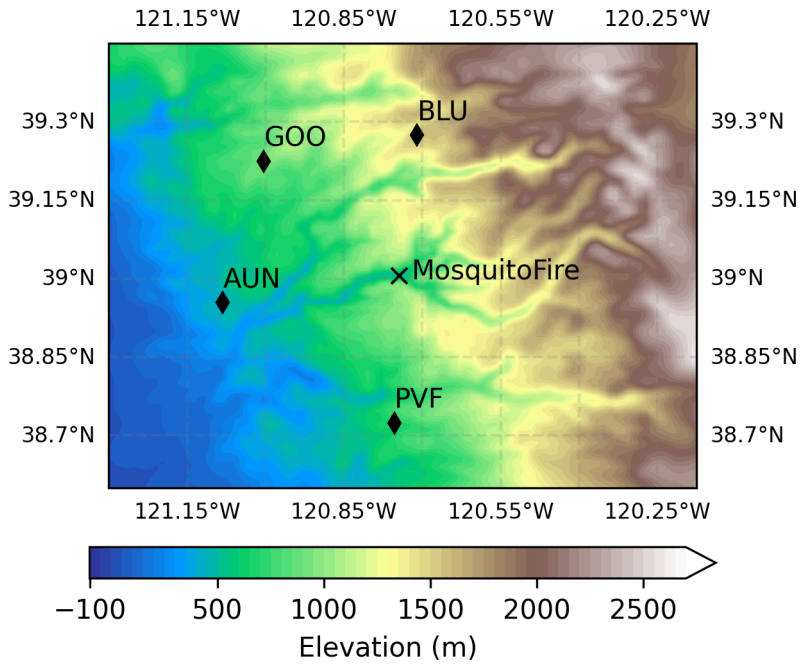


Figure 3. ASOS station locations in WRF D02.

Figure 5 presents correlation (scatter) plots comparing WRF-simulated surface meteorological variables against ASOS observations for stations within domain D02, with each subplot corresponding to a different near-surface variable: 2 m temperature (Figure 5a), 2 m (Figure 5b) relative humidity, 10 m wind speed (Figure 5c), and 10 m wind direction (Figure 5d). In each panel, the horizontal axis represents ASOS observations, and the vertical axis represents WRF output, with the 1:1 line indicating perfect agreement.

Although near-surface discrepancies in wind speed magnitude are evident and consistent with the surface wind speed bias identified in Figure 5, agreement improves substantially above the lowest atmospheric levels. This behavior is expected, as aircraft-based measurements are less influenced by local surface roughness and unresolved terrain effects than ground-based observations. Importantly, the model accurately captures the vertical wind shear profile, a key control on plume tilt, entrainment, and downwind transport.

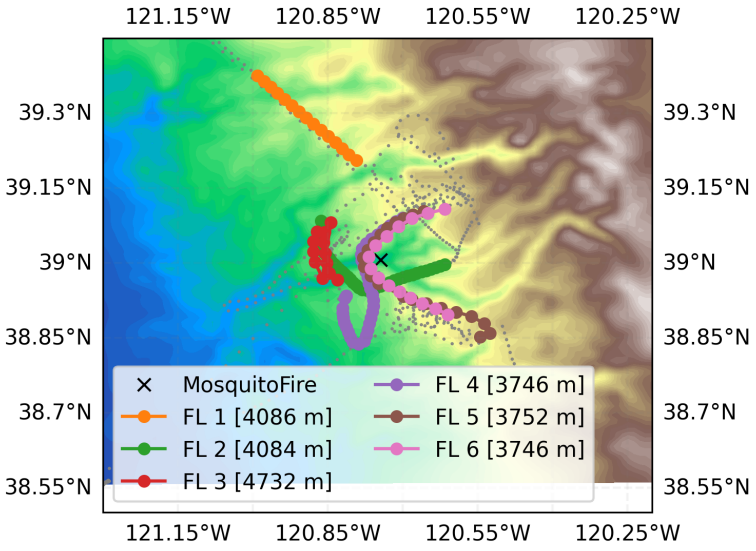


Figure 4. NOAA-Met Twin Otter flight legs in WRF D02 domain. The value in the paranthesis represents the average flight altitude for the flight leg (FL).

Taken together, Figure 5 supports the conclusion that WRF provides a reliable representation of the background ABL thermodynamic state and flow direction, which are the primary controls on plume advection and vertical coupling, while acknowledging known limitations in simulating near-surface wind speed magnitudes over complex terrain. This level of agreement is sufficient for initializing the finer-scale LES plume.

Figure 6 compares vertical profiles of wind speed from the WRF D02 simulation with in situ observations from the NOAA-MET Twin Otter (MET-TO) for multiple flight legs conducted over the Mosquito Fire region. Each panel corresponds to a different flight leg and time, with gray symbols representing MET-TO measurements, red curves showing the WRF-simulated mean wind profiles, and thin red envelopes indicating model variability across nearby grid points.

Figure 6 demonstrates that WRF captures the vertical structure and magnitude of winds throughout much of the atmospheric boundary layer and into the lower free troposphere, including the presence of enhanced wind speeds near and above the inversion layer. In particular, the model reproduces (i) the gradual increase of wind speed with height within the ABL, (ii) the development of stronger winds aloft associated with regional forcing and low-level jet-like features, and (iii) the timing and vertical placement of these features across successive flight legs.

Unlike the surface wind speed, the model simulated wind profiles match closely with the wind profiles observed by MET-TO, especially the WRF model, which was able to capture the variations in wind speed magnitude and wind direction profiles (Figures 6 and 7). Capturing these variations is critical for proper plume dispersion above the boundary-layer, as it is sensitive to local shear and/or wind direction shear. The boundary layer height diagnosed from the wind speed profiles from flight legs (FL) 4 and 6, which is around 1300 m, matches closely with the boundary layer height estimated from the backscatter profiles collected by MET-TO.

Overall, an independent upper-air validation of the WRF-simulated ABL structure has been conducted, demonstrating that the model realistically captures the wind profiles and shear relevant for smoke plume evolution, thus justifying its use for initializing the subsequent high-resolution LES plume simulations.

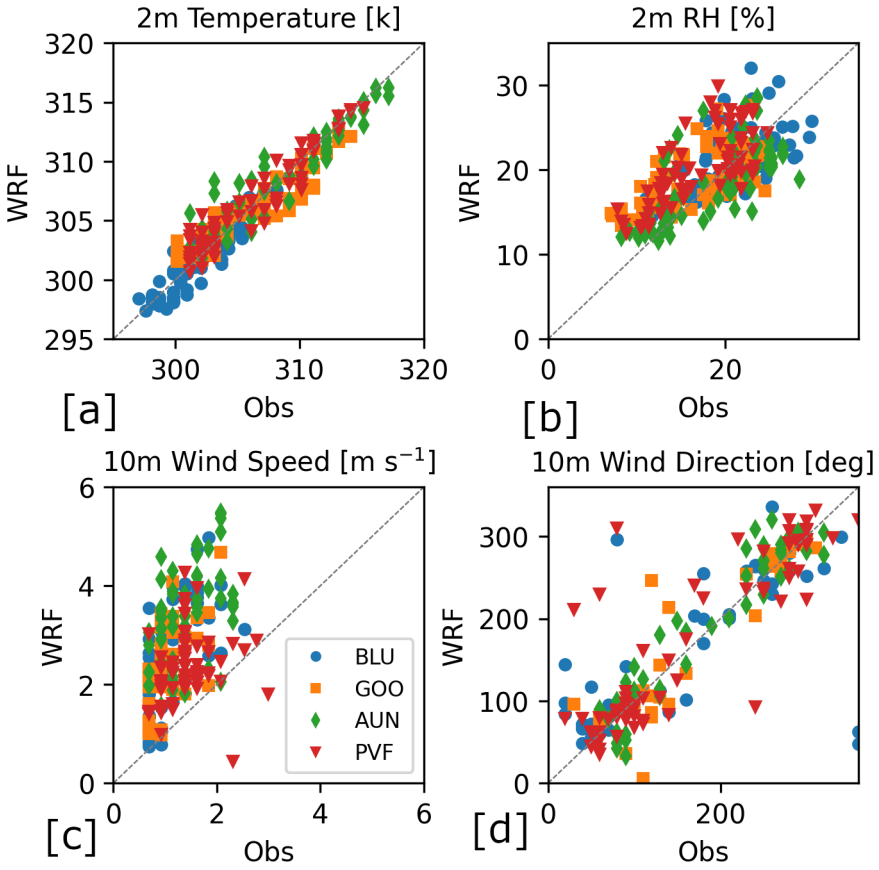


Figure 5. Correlation plot between WRF output and ASOS observed values for surface MET fields. The variable compared is mentioned in the title of the subplot.

It should be noted that Figures 5 and 6, however, reveal a systematic wind speed bias when compared with measurements from the MET-TO tower. Such discrepancies are not unexpected and can be attributed to several factors. Tower-based wind speed measurements are sensitive to local surface roughness, unresolved terrain heterogeneity, and sub-grid obstacles, which tend to reduce observed wind speeds relative to model grid-cell averages. In addition, differences between the anemometer height and the model's lowest prognostic levels can introduce apparent biases, particularly under stable or weakly convective boundary-layer conditions. Wind direction measurements are generally less sensitive to these local effects, explaining their comparatively better agreement.

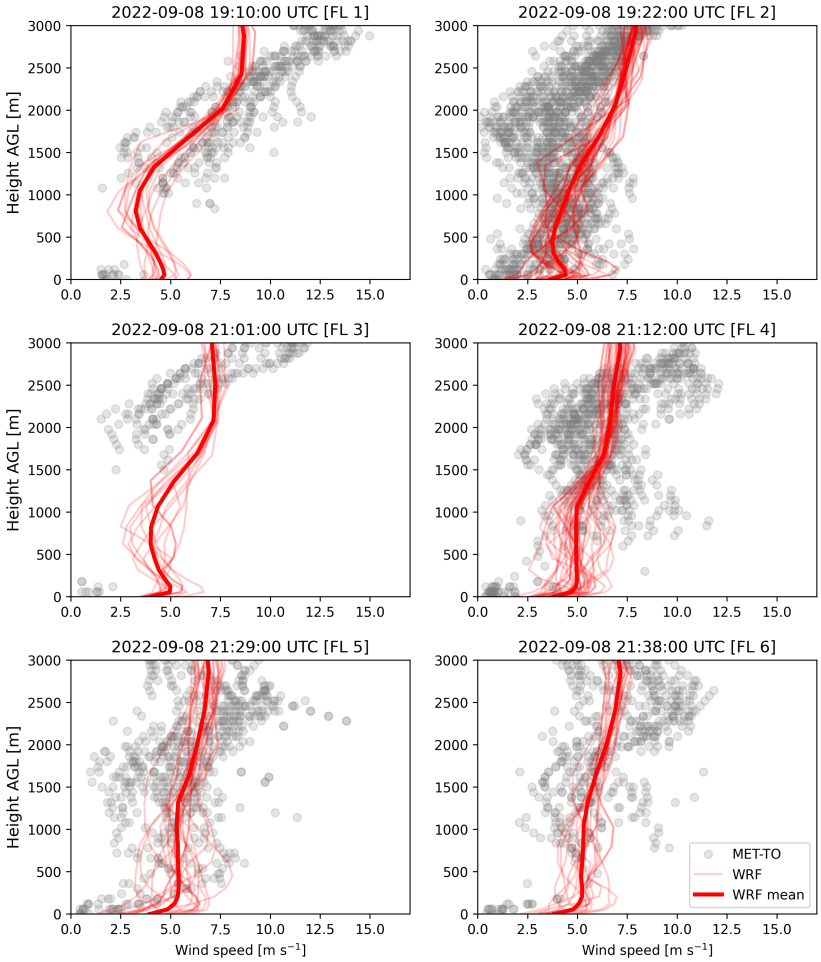


Figure 6. Wind speed profiles in WRF D02 compared against the MET-TO observations. The solid line corresponds to the WRF output and the symbols (dot) correspond to the MET-TO station data.

An additional and independent validation of the ABL structure is provided by the diagnosed boundary-layer height. The boundary-layer depth inferred from wind speed profiles obtained during flight legs FL4 and FL6 is approximately 1300 m, which closely matches the boundary-layer height estimated from the aerosol backscatter profiles collected at MET-TO. This consistency across airborne in situ measurements and remote-sensing diagnostics indicates that the vertical extent and bulk structure of the ABL are realistically represented, despite the presence of wind speed biases.

Taken together, these results indicate that while WRF exhibits systematic errors in wind speed magnitude near the surface, it captures the directional consistency, vertical structure, and boundary-layer depth that are most critical for plume transport. As shown in Figure 7, WRF reproduces the observed wind direction with good agreement throughout much of the boundary layer. This indicates that the model captures the dominant synoptic and mesoscale forcing responsible for organizing the mean flow, which is particularly important in complex terrain where channeling and terrain-induced circulations control plume advection pathways. Directional agreement, therefore, provides confidence that the simulated plume is advected along physically realistic trajectories.

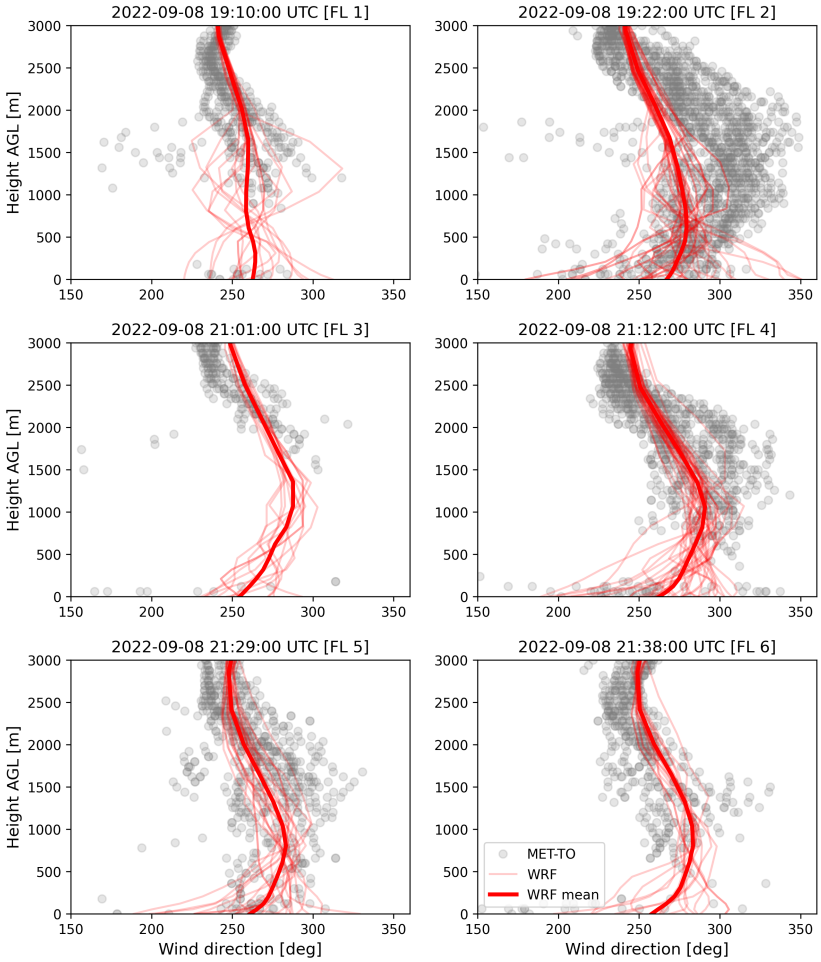


Figure 7. Wind direction profiles in WRF D02 compared against the MET-TO observations.The solid line corresponds to the WRF output and the symbols (dot) correspond to the MET-TO station data.

Table 2. Performance metrics for surface variables at individual ASOS stations shown in Figure 3.

ASOS Station	MET Variable	MAE	MBE	RMSE	R	*n*
BLU	T2 [°K]	0.91	−0.23	1.1	0.93	72
	RH2 [%]	3.10	0.44	3.80	0.56	72
	U10 [m/s]	1.45	1.44	1.67	0.60	61
	UDir10 [°]	44.1	3.03	78.6	0.56	49
GOO	T2 [°K]	1.29	−0.21	1.56	0.94	72
	RH2 [%]	3.55	1.91	4.35	0.64	72
	U10 [m/s]	1.34	1.35	1.50	0.44	39
	UDir10 [°]	29.9	−1.93	42.9	0.50	60
ANU	T2 [°K]	1.11	0.28	1.52	0.96	72
	RH2 [%]	3.06	−0.21	3.85	0.72	72
	U10 [m/s]	2.23	2.23	2.19	0.43	64
	UDir10 [°]	21.9	5.69	26.7	0.85	60
PVF	T2 [°K]	0.96	0.24	1.23	0.96	72
	RH2 [%]	3.93	3.32	4.68	0.73	72
	U10 [m/s]	1.02	0.93	1.18	0.25	69
	UDir10 [°]	30.5	6.58	52.2	0.85	69

Table 3. Performance metrics for surface variables averaged across ASOS stations shown in Figure 3.

MET Variable	MAE	MBE	RMSE	R
T2 [°K]	1.07	0.02	1.35	0.95
RH2 [%]	3.41	1.36	4.17	0.66
U10 [m/s]	1.46	1.43	1.63	0.43
UDir10 [°]	31.6	3.35	50.1	0.69

4. Analysis of the Atmospheric Boundary Layer

Turbulence within the atmospheric boundary layer is generated through the combined effects of buoyancy and shear, arising from surface heat exchange between the atmosphere and the Earth's surface, and from the interaction of the wind with surface roughness. Turbulent kinetic energy is produced by wind shear both near the surface and at the inversion layer, while buoyancy production associated with the mean temperature gradient or surface sensible heat flux contributes positively during unstable ABL regimes and negatively during stable conditions. The relative contributions of shear- and buoyancy-driven turbulence are quantified by the Monin-Obukhov length L, which represents the ratio of shear to buoyancy production of TKE and is defined as

$$L = \frac{-u_\star^3 \theta}{\kappa g \overline{w'\theta'}}, \tag{6}$$

where $u_\star$ is the friction velocity, κ is the von Karman constant, g is the gravitational acceleration, θ is the mean potential temperature, and $\overline{w'\theta'}$ is the surface kinematic heat flux [58–61].

The velocity scale associated with shear-driven turbulence is the friction velocity $u_\star$, while the velocity scale associated with buoyancy-driven motions is the convective velocity $w_\star$, defined based on the surface heat flux following Deardorff [62]. ABL regimes are classified using the stability parameter $\zeta = z_I/L$, where z_I is the inversion height, along with the ratio $u_\star/w_\star$, consistent with established regime classification frameworks [36,63]. In this framework, a buoyancy-dominated convective boundary layer is characterized by $\zeta \lesssim -40$ and $u_\star/w_\star \lesssim 0.25$, indicating that the buoyant production of turbulence strongly exceeds shear production. A shear-buoyancy regime is identified for intermediate conditions ($-40 \lesssim \zeta \lesssim -10$ and $0.25 \lesssim u_\star/w_\star \lesssim 0.6$), in which both shear and buoyancy contribute comparably to turbulence generation. A near-neutral, shear-dominated regime corresponds to $\zeta \gtrsim -10$ and $u_\star/w_\star \gtrsim 0.6$, where shear production dominates despite weak convective instability.

During the analysis period from 5 p.m. local time (LT = UTC−7) on 8 September to 3 p.m. LT on 9 September (Table 4), the Monin-Obukhov length remains negative, indicating persistently convective conditions. However, the magnitude of ζ and the ratio $u_\star/w_\star$ vary substantially, enabling robust regime discrimination. Weakly convective to buoyancy-dominated conditions prevail during the late evening hours of 8 September (5–7 p.m. LT), whereas increasing regional wind forcing after sunrise on 9 September elevates $u_\star$ and shifts the ABL into a shear-buoyancy regime between 5 a.m. and 3 p.m. LT. This transition from a buoyancy-dominated to a shear-buoyancy regime during the fire period has a direct impact on plume transport, as enhanced shear increases horizontal plume spreading while buoyancy continues to control vertical mixing within the ABL.

Table 4. Characteristics of the atmospheric boundary layer between 5 p.m. 8 September and 3 p.m. 9 September. Hourly averaged statistics for inversion height z_I (m), Monin-Obukhov's length L (m), atmospheric stability parameter $\zeta = \frac{z_I}{L}$, friction velocity $u_\star$ (m/s), convection velocity $w_\star$ (m/s).

Time	z_I (m)	L (m)	$\zeta = \frac{z_I}{L}$	$u_\star$ (m/s)	$w_\star$ (m/s)
5 p.m. 09/08	1502	−17	−88	0.22	1.18
7 p.m. 09/08	1502	−22	−68.3	0.24	1.18
9 p.m. 09/08	528	−41	−12.8	0.29	1.08
11 p.m. 09/08	379	−64	−5.9	0.34	1.07
1 a.m. 09/09	162	−68	−2.4	0.34	0.88
3 a.m. 09/09	162	−71	−2.3	0.35	0.89
5 a.m. 09/09	258	−107	−2.41	0.4	1.08
7 a.m. 09/09	379	−183	−2	0.48	1.01
9 a.m. 09/09	711	−201	−3.5	0.41	1.29
11 a.m. 09/09	932	−272	−3.4	0.4	1.47
1 p.m. 09/09	1195	−281	−4.2	0.56	1.49
3 p.m. 09/09	1502	−105	−14.3	0.4	1.48

In canonical flat-terrain boundary layers, convection typically intensifies during the daytime as surface heating strengthens buoyancy, while vertical wind shear and jet-like features become more prominent at night following the collapse of turbulence and the development of a stable boundary layer. In complex terrain, however, topographically driven circulations and terrain-induced pressure gradients can substantially modify this classical diurnal cycle, leading to departures from the expected timing and vertical distribution of shear. The behavior discussed below should therefore be interpreted in the context of the highly inhomogeneous topography of the present domain, which plays an active role in shaping the ABL structure.

Statistical averages are computed relative to the local topographic surface, which is defined as the zero-elevation reference. The terrain within the numerical domain is highly inhomogeneous, with elevations ranging from approximately 400 m to 1600 m (see Figure 2). Hourly-averaged mean horizontal and vertical wind speed profiles during the early morning hours of 9 September are shown in Figure 8a and Figure 8b, respectively, while the corresponding daytime mean horizontal wind speed and temperature profiles are presented in Figure 8c,d.

During the early morning period (01:00–05:00 a.m.), the mean horizontal wind-speed profile exhibits a pronounced low-level wind maximum located within the lowest few hundred meters above ground level, consistent with the formation of a nocturnal low-level jet (LLJ). This near-surface wind maximum is accompanied by enhanced vertical shear confined to a shallow layer close to the surface, as evident in both the mean horizontal and vertical velocity profiles (Figure 8a,b). At 7 p.m. on 8 September, the vertical wind shear is concentrated near the inversion layer, while winds remain relatively weak close to the surface. As the night progresses into the early morning hours of 9 September, the shear near the inversion weakens, and the horizontal wind maximum shifts downward toward the surface, producing a narrow layer of strong near-surface shear.

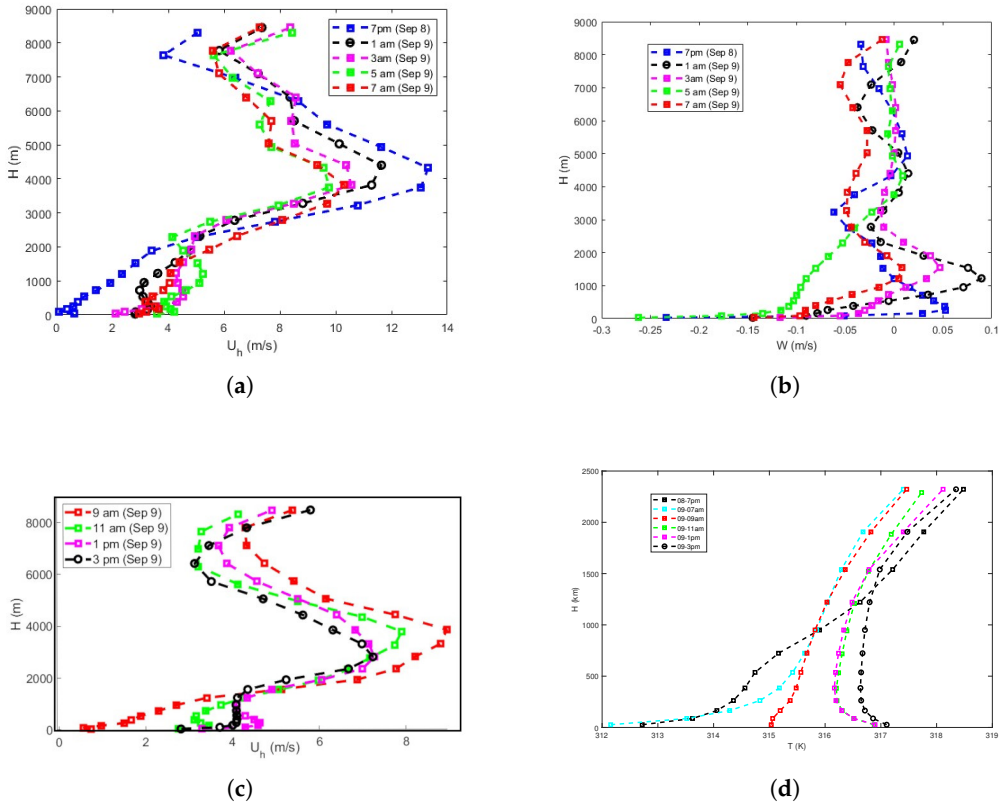


Figure 8. During the early morning hours of 9 September the hourly averaged profiles of (**a**) horizontal wind speed profiles, (**b**) vertical wind speed profiles, (**c**) mean horizontal wind speed profiles, (**d**) mean temperature profiles.

From mid-morning onward (after approximately 9 a.m.), surface heating produces a negative near-surface temperature gradient, leading to the development of convective conditions within the ABL and an increase in vertical shear throughout the layer. The peak daytime horizontal wind speed within the ABL reaches approximately 5 m s^{-1}, while surface temperatures rise to nearly 317 K due to solar heating. By mid-afternoon (3 p.m.), a well-developed mixed layer is established. Above the ABL, within the inversion layer at approximately 3–4 km above ground level, the regionally imposed horizontal wind strengthens into an elevated jet-like structure, with wind speeds approaching 9 m s^{-1} (Figure 8c). Enhanced shear is present both below and above this elevated wind maximum. Above the inversion layer, wind speeds decrease before increasing again toward geostrophic values in the free troposphere.

The increase in near-surface vertical velocity during the early morning hours is consistent with the presence of a nocturnal LLJ, which commonly forms near the top of the stable boundary layer. In California, coastal low-level jets have been linked to baroclinic forcing, in which geostrophic adjustment and thermal wind balance produce a wind-speed maximum above the surface layer [64]. Topography further modulates these jets through coastline curvature and terrain blocking and plays a dominant role in the formation of barrier jets along major mountain ranges such as the Sierra Nevada [65]. Although a clear jet-like structure is present during the early morning hours in both the horizontal and vertical wind components, the magnitude of the jet ($\sim$5–9 m s^{-1}) is weaker than that associated with strong coastal jets and is consistent with nocturnal LLJs documented over inland valleys and complex terrain [66]. In the next section, we examine the extent to which domain averaging and topographic heterogeneity influence the diagnosed jet strength.

In Figure 9, the wind speed in the $x - z$ plane is plotted to highlight the influence of topography on the spatial variation of wind speed. At 5 p.m. on 9 September, the wind is relatively constant across the entire domain, as seen in Figure 9a. Figure 9b–d show the wind speed at 1 a.m., 3 a.m., and 5 a.m. on 9 September, respectively. During the early morning hours, topography plays a strong role in creating significant gradients across the terrain. Jet-like behavior dominates on the western side of the domain. The effects of topography and the jet-like behavior generate turbulence mechanically during the night. This is also expected, as many studies indicate strong topographic effects during stable conditions [67].

Contour plots of the hourly averaged vertical velocity fields in the $x - z$ plane are shown in Figure 10. At 5 p.m. on 8 September (Figure 10a), intermittent (in space) strong shear layer uplift is identified close to the surface. The formation and confinement of these structures are consistent with the early-morning LLJ and near-surface shear layer diagnosed from the mean profiles in Figure 8. This structure strengthens between 5 p.m. and 11 p.m. as $u_\star$ begins to increase (Figure 10a–d). The flow field is dominated by strong updrafts and down-drafts that extend to 6 km above the surface (Figure 10b–d). During these times, the ABL is strongly convective, with vertical shear instabilities dominating the transport processes. A clear pattern of alternating updrafts and downdrafts is formed from 5 a.m. onward. Starting at 5 a.m. on 9 September (Figure 10g–l), well-defined updrafts and downdrafts are evident close to the surface. They extend up to a height of 2 km above the surface.

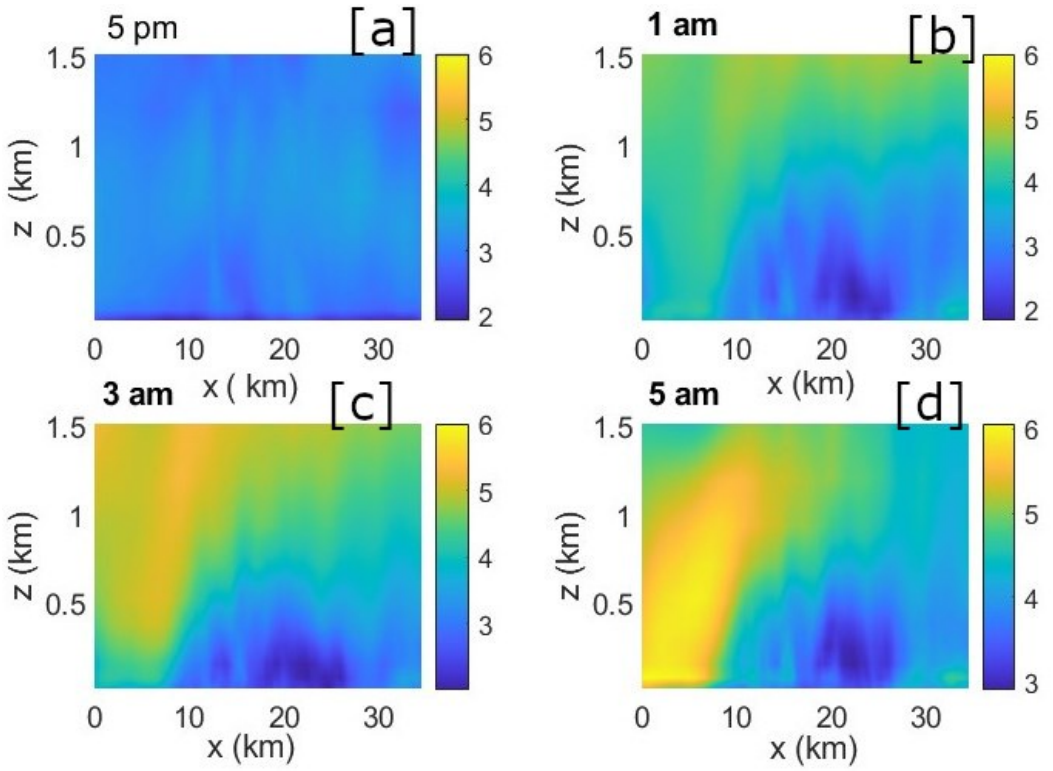


Figure 9. Contour plot of the wind speed (m/s) plotted in the $x - z$ plane for the D03 domain at (**a**). 5 p.m. (8 September), (**b**). 1 a.m. (9 September), (**c**). 3 a.m. (9 September), (**d**). 5 a.m. (9 September).

The horizontal velocity field in the $x - y$ plane at 30 m above the surface at 1 p.m. on 9 September is shown in Figure 11a. The flow field is characterized by a pattern of high-speed and low-speed elongated streaks. Above this level, the streaks become less organized, and the spacing between them increases with height, as might be expected

from the discussion of Figure 12. The horizontal velocity in the $x-z$ plane sampled at the middle of the y dimension at 1 p.m. on 9 September is shown in Figure 11b. The ABL is in the shear-buoyancy regime, with winds varying between 4 and 6 m/s, indicating strong shear within the boundary layer to a height of 1.5 km above the surface. The winds are generally even stronger within the inversion layer, which extends up to 5 km. Above 5 km, winds diminish to the top of the inversion layer. It should be noted that horizontal streaks are not evident (at all heights) until the horizontal winds pick up around 5 a.m. on 9 September. Overall, the flow structures reveal the presence of three dynamically distinct regions: the ABL, which is below the inversion layer; the inversion layer; and the region above the inversion layer. Within the ABL, buoyancy driven turbulent mixing dictates the flow field, which is characterized by alternating strong updrafts and downdrafts that contribute to the vertical transport of momentum, heat, and species. Within the inversion layer, there is a strong shear-layer produced by strong horizontal winds, and above the inversion layer, the winds are governed by slower geostrophic winds.

The turbulent kinetic energy is analyzed next. The hourly averaged TKE in the $x-z$ plane is given in Figure 12. Figure 12a shows the TKE at 5 p.m. on 8 September. Two distinct regions of high TKE are observed: The first is at a height of 2 km above the surface, generated primarily by horizontal wind shear at the bottom of the inversion layer (Figure 8). The second region is defined by TKE generated close to the surface, primarily by buoyant convection. However, the near-surface TKE magnitude at this time is much lower than that at 2 km. As time progresses, the intensity of TKE at 2 km diminishes, and the near-surface TKE becomes stronger (Figure 12b–f). The region of high TKE on 9 September extends up to 500 m above the surface.

By early afternoon (1 p.m.), the turbulent kinetic energy (TKE) increases and extends to a depth of approximately 2 km (Figure 12j), indicating enhanced turbulent mixing and entrainment throughout the ABL. This increase in TKE arises from the simultaneous action of shear-generated and buoyancy-generated turbulence. During this period, the mean vertical temperature gradient is negative ($\partial\theta/\partial z < 0$) within the mixed layer, corresponding to an unstable stratification produced by strong surface heating. Under such conditions, buoyancy acts as a source of turbulence by accelerating warm air parcels upward and cool air parcels downward, resulting in positive buoyancy production of TKE.

In the presence of a negative temperature gradient, buoyancy production does not oppose the mean shear; instead, it reinforces shear-generated turbulence. Consequently, both shear and buoyancy terms in the TKE budget contribute positively, leading to elevated TKE levels and deeper vertical mixing [60,61]. In contrast, during early morning or nighttime conditions, when the temperature gradient is weakly negative or becomes positive (stable stratification), buoyancy acts to suppress vertical motions and counteracts shear-generated turbulence. This competition between shear and buoyancy reduces net TKE production and limits vertical mixing, resulting in a shallower and more weakly turbulent boundary layer.

In conclusion, shear associated with anticyclonic flow within the inversion layer promotes the accumulation of turbulent kinetic energy (TKE) during the late evening and early morning hours. During this period, buoyancy-driven turbulence is weak, and turbulence production is dominated by mechanically generated shear near the inversion. As the day progresses and surface heating intensifies, the boundary layer deepens and transitions toward a regime influenced by cyclonic flow. Under these conditions, enhanced mixing and turbulence production occur throughout the interior of the boundary layer, redistributing TKE away from the inversion and into the mixed layer. The evolving interplay between anticyclonic shear near the inversion and cyclonic influences during the daytime ultimately governs the magnitude and vertical distribution of turbulence within the boundary layer.

The characteristics of the ABL between 5 p.m. on 8 September and 3 p.m. on 9 September have been analyzed using the WRF-LES simulations. The results demonstrate that the ABL is in a weakly convective regime from 5 p.m. on 8 September to 3 a.m. on 9 September; subsequently, the ABL transitions to a shear-buoyancy regime. During this period, the ABL height deepens to a maximum height of 1.2 km. Around the time when the smoke plume is introduced (noon on 9 September), strong ABL turbulence develops within the boundary layer due to solar heating; additionally, the regionally imposed horizontal wind has also increased. During the shear-buoyancy regime (morning/late afternoon), the turbulence consists of strong updrafts and down-drafts in the vertical-planes, with a clear pattern of alternating high-speed and low-speed streaks in the horizontal plane. Two distinct regions of high TKE are observed: The first is at the inversion layer, which is at a height of 2 km above the surface. In this region, the TKE is generated primarily by horizontal wind shear. The second region is in the near-surface region, where the TKE is generated primarily by buoyant convection. The relative strength of the TKE between the inversion layer and the near-surface region varies at different instants of the diurnal cycle. During the morning/afternoon hours of 9 September, TKE is higher in the near-surface region than at the inversion height. However, on the previous night, between 11 p.m. and 1 a.m., a higher TKE is generated at the inversion layer than in the near-surface region. The vertical structure becomes more organized and extends up to approximately 4 km over the entire domain. It is likely that warm air from the inversion layer is being pushed down while cooler air ascends. As the ground cools, the temperature difference between the inversion height and the surface increases. The turbulence is low during this period, and there is not much mixing, resulting in elongated structures indicating that warm columns of air are descending. Between 1 a.m. and 5 a.m., a localized low level jet develops, producing mechanical turbulence close to the surface and thus enhancing turbulence during this time. Topographic effects are also significant during this time, resulting in apparent spatial inhomogeneity.

At this stage of the analysis, the focus remains on characterizing the atmospheric boundary layer regimes identified in Section 3. To clarify how differences in ABL structure translate into differences in vertical and horizontal transport, we introduce a regime-based sensitivity summary (Table 5). The table does not present plume simulation results but rather synthesizes how variations in plume response arise from differences in ABL depth, stability, shear, and turbulence under identical, observationally constrained forcing. In this sense, the plume serves as a diagnostic of the ABL state.

Table 5 shows the plume sensitivity in terms of the observed ABL regimes diagnosed from the WRF-LES ABL simulation. The table identifies how changes in ABL depth (z_I), stability ($\zeta = z_I/L$), and the relative importance of mechanical and buoyant turbulence ($u_\star/w_\star$) alter the expected plume response. The nocturnal period is characterized by a shallow boundary layer and an LLJ-driven near-surface shear maximum, conditions that favor rapid horizontal advection and lateral spreading while suppressing sustained vertical penetration. After sunrise, mixed-layer growth increases z_I and buoyant mixing; however, increasing shear enhances entrainment near the inversion, shifting control toward the combined effects of inversion-layer turbulence and winds aloft. The plume-release hour (1 p.m.) occurs in a shear-buoyancy regime, for which plume-top height is governed primarily by z_I and inversion-layer mixing, while horizontal transport is amplified once plume material reaches the upper ABL and lower free troposphere, where winds are stronger.

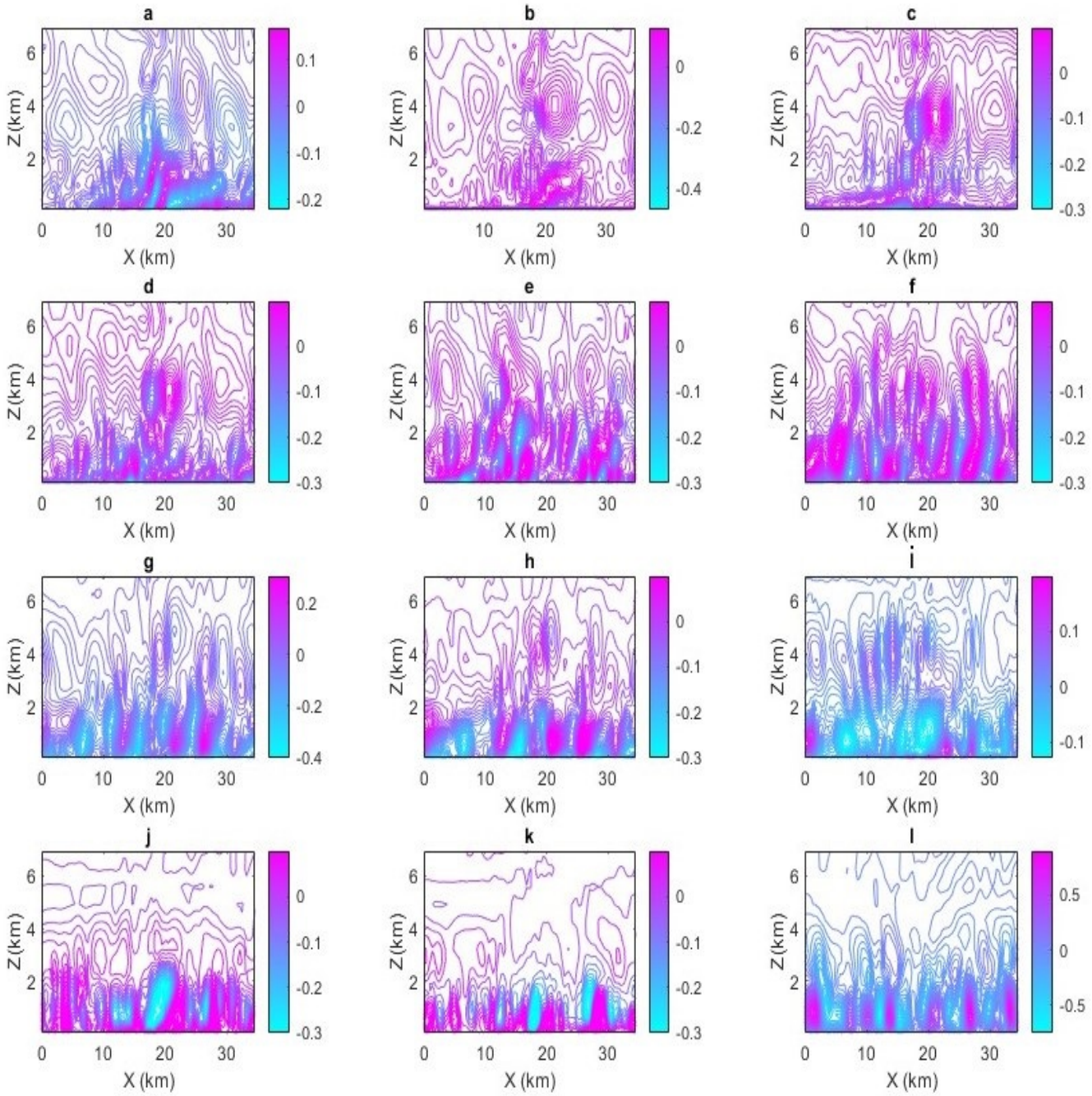
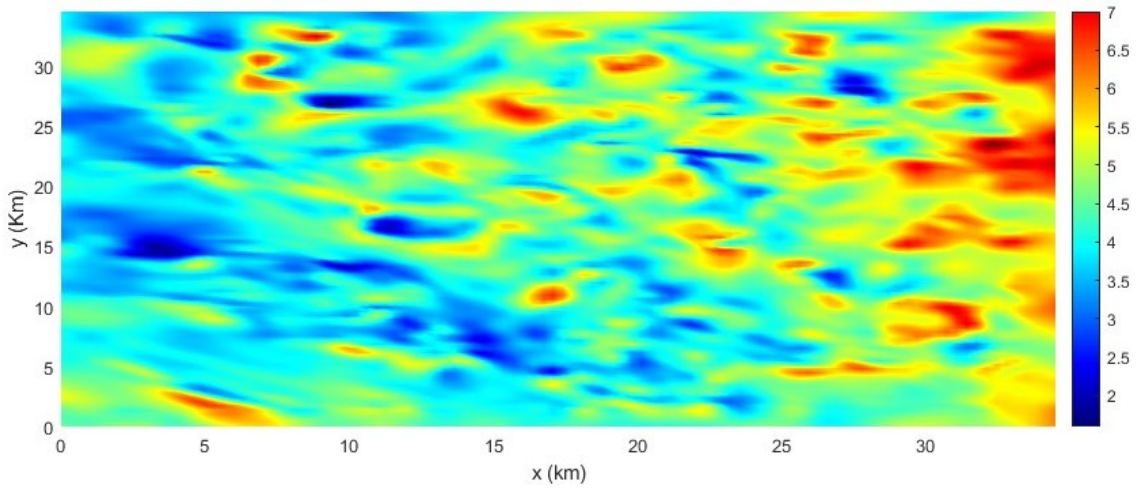
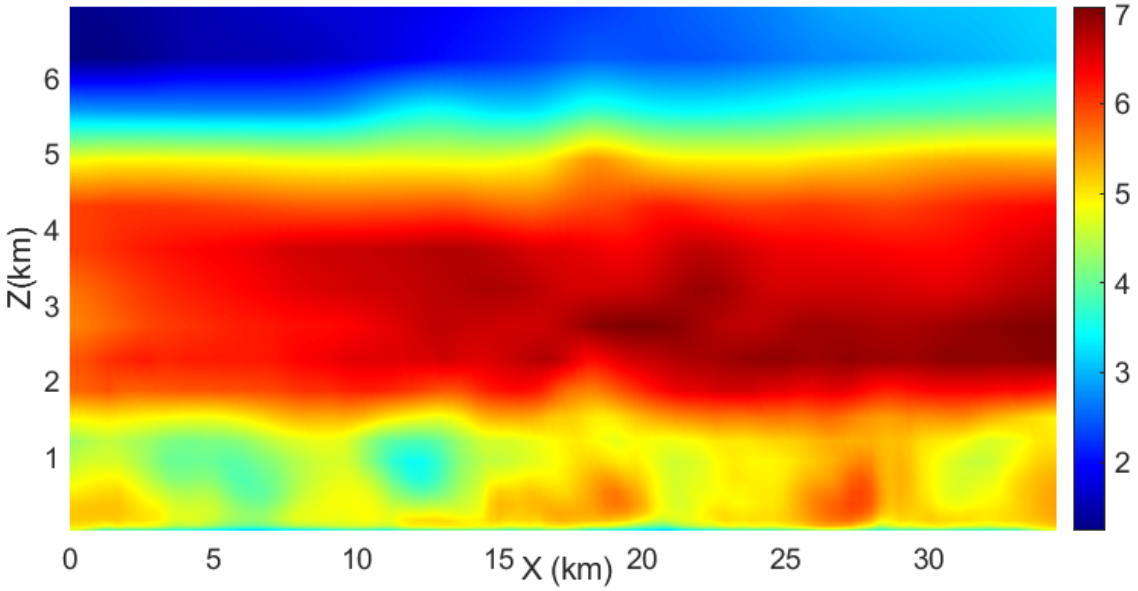


Figure 10. Contour plot of the simulated vertical velocity of the plume, sampled in the $x - z$ plane for the D03 domain during 8–9 September at (**a**). 5 p.m., (**b**). 7 p.m., (**c**). 9 p.m., (**d**). 11 p.m., (**e**). 1 a.m., (**f**). 3 a.m., (**g**). 5 a.m., (**h**). 7 a.m., (**i**). 9 a.m., (**j**). 11 a.m., (**k**). 1 p.m., (**l**). 3 p.m. Note the scale changes from panel to panel. Note the aspect ratio of the figure has been altered for clarity of the structures.



(**a**)



(**b**)

Figure 11. The contour plot of the horizontal velocity at 1 p.m. on 9 September (**a**). (**top figure**) Sampled in the horizontal plane, $x - y$ at $z = 30$ m above the surface. (**b**). (**lower figure**) Sampled in $x - z$ plane at the mid-surface.

Table 5. Regime-based sensitivity of buoyant plume response to atmospheric boundary layer structure during the Mosquito Fire.

ABL Regime (LT)	Stability Metrics	Dominant ABL Features	Implications for Plume Transport
Buoyancy-dominated CBL	$z_I \sim 1.5$ km, $\zeta \ll 0$, $u_\star / w_\star \sim 0.2$	Deep mixed layer; buoyancy-driven turbulence.	• Strong vertical mixing • Plume rise limited by z_I • Weak shear-driven spreading
Evening transition	$z_I \sim 0.5$ km, $\zeta \approx -10$	Collapsing ABL; strengthening inversion.	• Reduced vertical penetration • Increased inversion entrainment • Growing shear influence

Table 5. *Cont.*

ABL Regime (LT)	Stability Metrics	Dominant ABL Features	Implications for Plume Transport
Nocturnal LLJ regime	$z_I \sim 150-250$ m, $u_\star/w_\star > 0.3$	Shallow layer; strong LLJ; intense shear.	• Vertical plume rise suppressed • Rapid horizontal advection • Strong lateral plume spreading
Morning growth	$z_I \sim 0.4-0.9$ km, $\zeta \approx -3$	Mixed-layer deepening; shear and buoyancy active.	• Gradual increase in plume rise • Enhanced inversion entrainment • Moderate horizontal transport
Plume-release period	$z_I \sim 1.2$ km, $\zeta \approx -4$, $u_\star/w_\star \sim 0.38$	Well-developed CBL; elevated winds aloft; high TKE near inversion.	• z_I constrains plume top • Partial lofting via inversion-layer TKE • Fast downwind transport aloft
Afternoon shear-buoyancy	$z_I \sim 1.5$ km, $\zeta \approx -14$	Deep CBL; strong shear; active entrainment.	• Higher plume tops possible • Increased dilution by entrainment • Strong shear-driven spreading

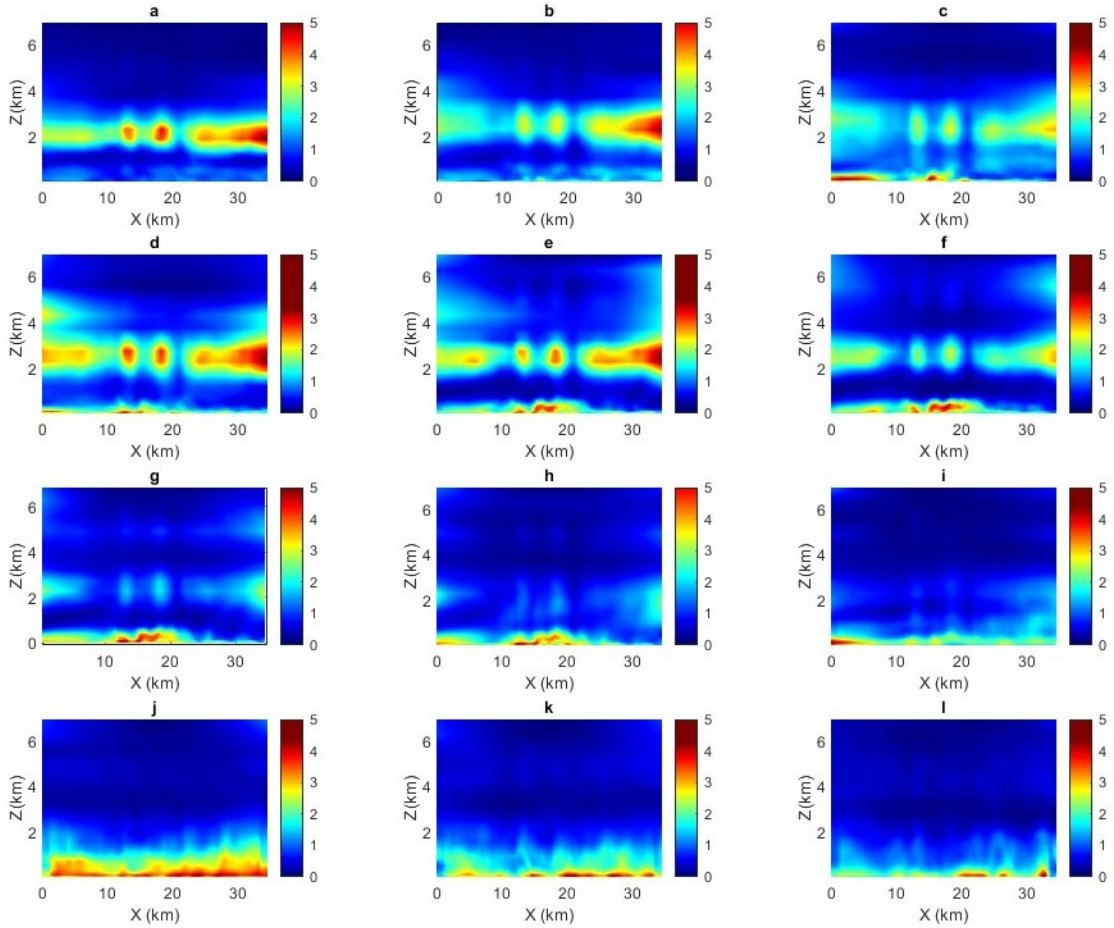


Figure 12. Contour plot of the Turbulent kinetic energy (TKE) sampled in the $x-z$ plane between 8–9 September plotted at (**a**). 5 p.m., (**b**). 7 p.m., (**c**). 9 p.m., (**d**). 11 p.m., (**e**). 1 a.m., (**f**). 3 a.m., (**g**). 5 a.m., (**h**). 7 a.m., (**i**). 9 a.m., (**j**). 11 a.m., (**k**). 1 p.m., (**l**). 3 p.m.

5. Plume Characteristics

The analysis of the plume is conducted next.

Figure 13 shows the temporal evolution of the plume in the $x - z$ plane over 50 min. Initially, the plume is similar to a jet; it transports vertically to a height of 2 km without significant mixing (Figure 13a–e). Beyond this height, mixing and entrainment are evident, and the plume expands radially outward (Figure 13a–f). The mixing results in the plume spreading horizontally and turning toward the surface (Figure 13h). This further intensifies with time, as seen in Figure 13i, as the plume spreads horizontally to a distance of 1.5 km.

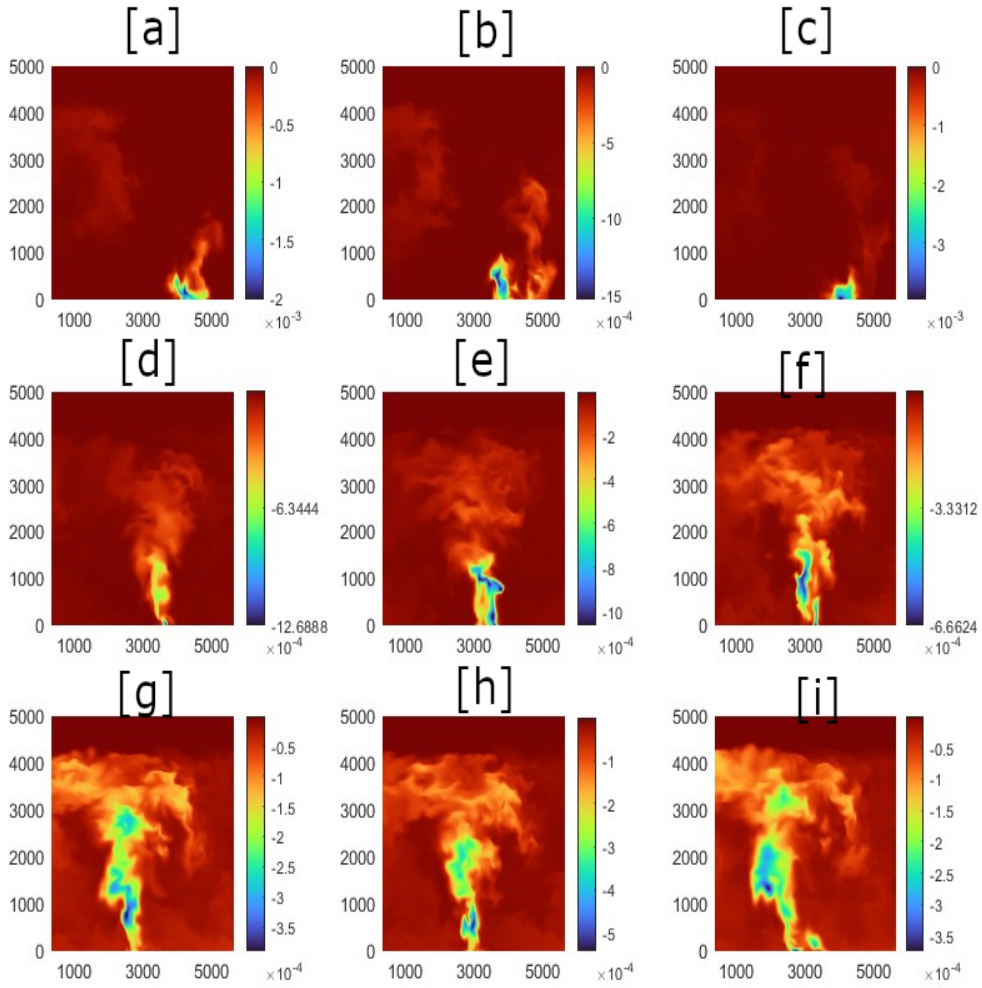


Figure 13. Contour plot of the plume concentration (kg/kg) sampled in the $x - z$ plane at times from the start of the plume release: (**a**). 10 min, (**b**). 20 min, (**c**). 25 min, (**d**). 30 min, (**e**). 40, (**f**). 35 min, (**g**). 40 min, (**h**), 45 min, (**i**). 50 min.

Figure 14 shows the plume transport and spread at different times in the $x - y$ plane (vertically averaged). Initially, the plume spreads radially 500 m away from the source (Figure 14a); subsequently, it extends horizontally close to 1 km downstream (Figure 14b). Furthermore, it transports in the cross-wind direction as well (Figure 14c,d). The plume behavior is closely related to the ABL characteristics. During plume injection, the ABL depth is around 1 km, and TKE is concentrated at a height of 2 km above the surface (as seen in Figure 12j). The vertical velocity consists of updrafts and downdrafts that carry the momentum and heat flux of the plume (as seen in Figure 10j). The vertical rolls extend to a depth of 2 km to 2.5 km above the surface. At plume release, the underlying ABL dynamics influence the vertical transport and horizontal spread. Furthermore, the evolution of the ABL over time controls the plume dynamics.

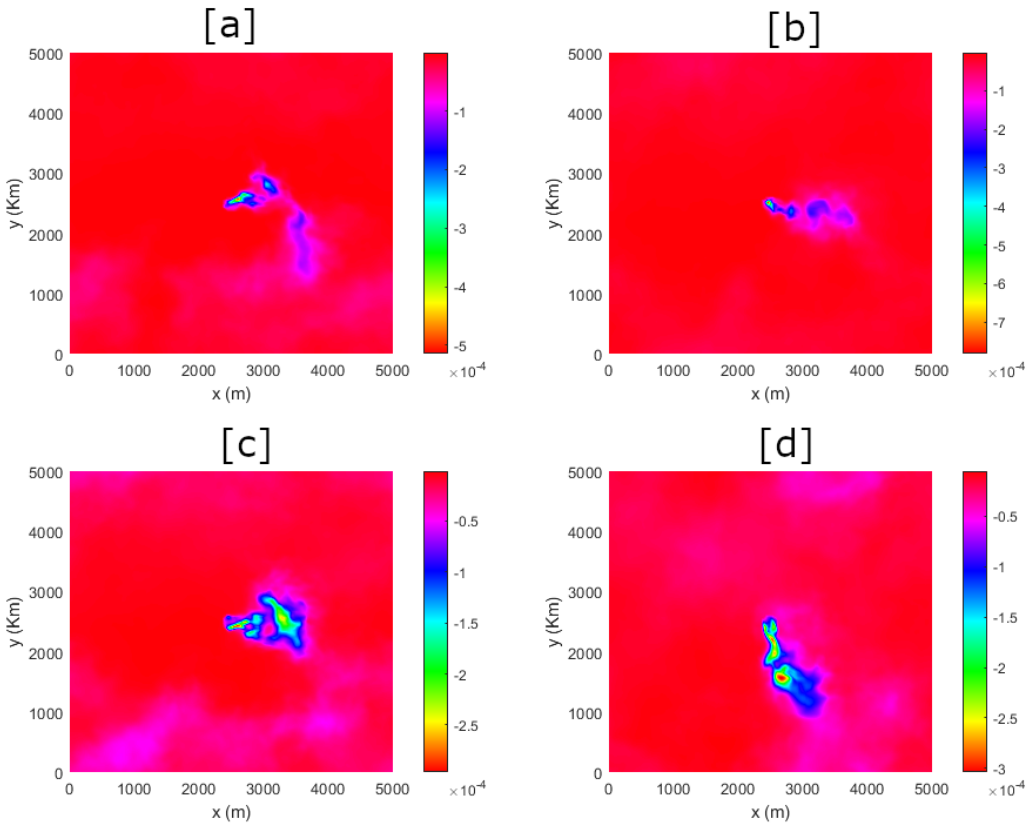


Figure 14. Contour plot of the plume concentration (kg/kg) sampled in the $x - y$ plane (averaged vertically) at times from the start of the plume release: (**a**). 20 min, (**b**). 30 min, (**c**). 40 min, (**d**). 50 min.

Temperature contours in the $x - z$ plane are shown in Figure 15. The interactions between the atmospheric turbulence and the plume turbulence are observed. During the onset of the plume, strong convective turbulence with turbulent bursts near the surface is evident (Figure 15a,b). At a later time, the higher plume temperatures reach a height of 1 km vertically and 500 m horizontally (Figure 15c). Plume mixing and dilution become stronger, altering the local temperature surrounding the plume (Figure 15d).

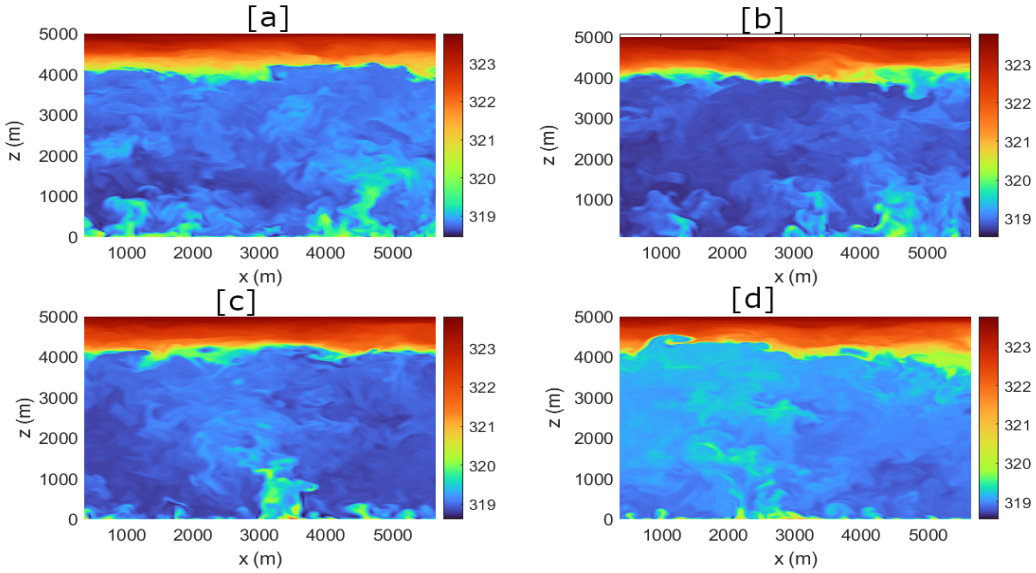


Figure 15. Contour plot of the plume Temperature field sampled in the $x - z$ plane at times from the start of the plume release: (**a**). 10 min, (**b**). 20 min, (**c**). 30 min, (**d**). 40 min.

5.1. Consistency of Plume Forcing and Vertical Structure with Satellite Imaging

The consistency of both the imposed plume forcing and the simulated plume rise is assessed through a comparison with satellite-based observations of fire intensity and plume vertical structure from the Moderate Resolution Imaging Spectroradiometer and the Multi-angle Imaging SpectroRadiometer (MISR), respectively. MODIS FRP provides a physically based constraint on the magnitude of surface heat release associated with the Mosquito Fire, while MISR offers one of the few spaceborne datasets capable of resolving plume-top heights, vertical structure, and wind shear using stereoscopic imaging. Together, these complementary datasets allow for the evaluation of whether the simulated plume forcing and its interaction with the ambient ABL are consistent with observed fire behavior and plume evolution.

MISR is a spaceborne instrument aboard NASA's *Terra* satellite that acquires near-simultaneous multi-angle observations in the visible and near-infrared spectral bands. By combining imagery from nine fixed viewing angles spanning forward, nadir, and aft directions, MISR stereo-imaging techniques enable the retrieval of plume heights, vertical structure, and horizontal wind shear through feature tracking across viewing geometries [68]. Although MISR overpasses represent discrete observation times, the stereo-retrieved plume heights implicitly integrate plume evolution over horizontal transport distances corresponding to approximately 6–8 h of advection in this case, based on the downwind extent of the visible plume and the retrieved MISR wind speed estimates (this is a measured value, not just an assumed, typical wind speed). These factors vary from plume to plume, so the MISR observed time horizons are different from 6–8 h for other plumes [14]. As discussed by Junghenn Noyes et al. [69], MISR plume heights therefore reflect a time-integrated record of plume rise, entrainment, and shear-driven transport rather than an instantaneous plume state.

Figure 16 shows MISR stereo-retrieved smoke plume heights on 8 September 2022 near 39.04° N, 120.76° W from two distinct viewing geometries, with plume altitude encoded by color. Both views reveal a consistent vertical plume structure, with near-source smoke largely confined below approximately 1 km above ground level and plume-top heights extending to approximately 4–5 km above ground level downstream. The spatial tilt and elongation of the plume indicate pronounced vertical wind shear, with distinct transport pathways within the ABL and in the flow aloft.

Using stereo feature tracking, MISR further retrieves horizontal wind vectors as a function of altitude. For the Mosquito Fire period, Noyes and Kahn [14] report relatively weak winds of approximately 2.8 m s^{-1} below 2 km above ground level, transitioning to stronger winds of about 4.7 m s^{-1} above this height. This vertical shear structure is consistent with the background wind profiles imposed in the present simulations. MISR analysis also indicates that the near-source plume resides at approximately 3 km above the surface, while smoke observed roughly 30 km downwind descends toward the surface, reflecting combined effects of shear-driven transport and entrainment.

The simulated plume evolution exhibits similar behavior. In the LES, the plume initially rises to approximately 3 km above the surface, with mixing extending to nearly 4 km during the first hour following plume injection. Downstream, the mixed layer expands and bends clockwise toward the surface as the plume encounters strong vertical wind shear. Winds of approximately 4.5 m s^{-1} are present within the lowest 2 km, increasing to about 6.5 m s^{-1} between 2 km and 4 km, resulting in rapid horizontal transport while the plume resides in the upper ABL and lower free troposphere, followed by reduced advection as the plume descends into the lower ABL.

The simulated plume-top heights, vertical gradients, and downstream spreading patterns shown in Figures 13–15 are consistent with the observed plume evolution. In both the MISR retrievals and the LES results, the plume is initially confined within the ABL near the source, followed by partial lofting into the upper ABL and lower free troposphere downstream. Elevated turbulent kinetic energy within this region further enhances mixing, while the combination of ABL depth, organized vertical motions near the inversion, and strong winds aloft governs plume rise and downstream transport. This agreement between satellite-derived plume structure and the simulated response to the resolved ABL dynamics supports the physical consistency of the imposed plume forcing and the fidelity of the modeled plume-ABL interaction, despite the limited temporal sampling of the satellite overpass.

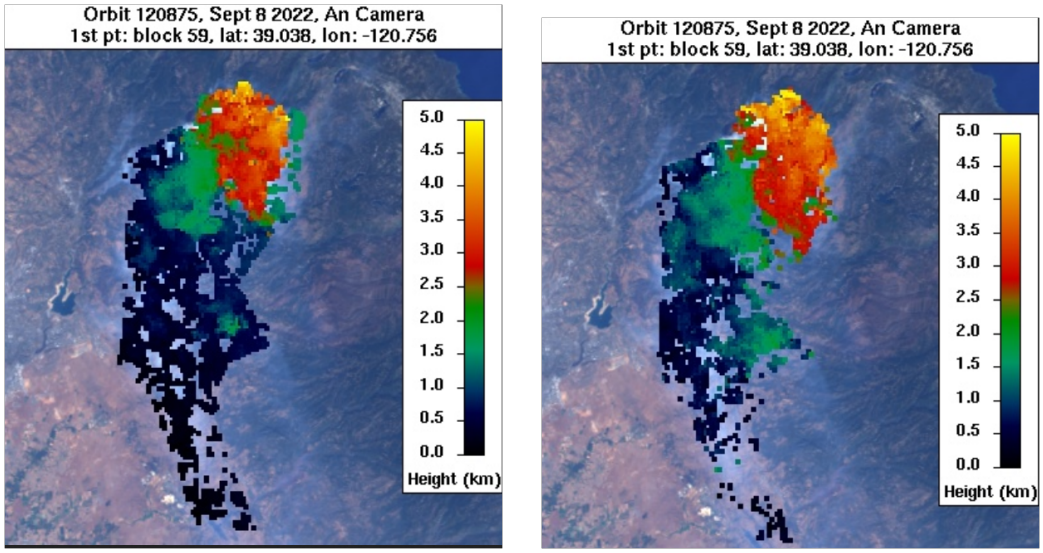


Figure 16. MISR stereo-retrieved smoke plume heights on 8 September 2022 (Orbit 120875, An camera) near 39.04° N, 120.76° W from two viewing geometries. Colors indicate plume height above ground level (km). These are available as supplementary material in [14].

5.2. Interpretation and Scope of Validation

The agreement between the MODIS-derived FRP, MISR plume heights, MISR-derived wind shear, and the LES results should be interpreted as consistency rather than exhaustive validation. The plume source parameters in the LES are not tuned to match the MISR observations, but the FRP from MODIS was applied as a model constraint; hence, the comparison is not intended to provide pointwise or time-resolved validation of plume dynamics. Instead, the combined MODIS and MISR observations provide independent assessments demonstrating that the imposed plume forcing and the simulated ABL-controlled plume evolution fall within the range supported by satellite measurements.

Taken together, these comparisons support the fidelity of the simulated ABL structure and its dominant role in governing plume rise, vertical mixing, and horizontal transport during the fire event, while acknowledging the idealized nature of the plume representation.

5.3. Sensitivity Results

Next, we assess plume-source sensitivity diagnostically within the ABL regimes resolved by the large-eddy simulations. This approach allows for the relative importance of plume forcing versus ABL structure to be evaluated in a physically interpretable framework.

In Table 6, the *columns* represent the distinct ABL regimes identified in Section 3, ranging from nocturnal shear-dominated conditions with LLJ to transitional shear-buoyancy regimes and a fully developed convective mixed layer. The *rows* correspond to perturbations in plume-source parameters, including source diameter, surface heat flux, buoyancy flux, and forcing duration. Each table entry summarizes the resulting plume response under the given ABL regime, highlighting how vertical penetration, entrainment, and horizontal transport jointly depend on plume forcing and the ambient ABL state.

The plume-source sensitivity summarized in Table 6 is interpreted through the governing relationship between source diameter, surface heat flux, and buoyancy flux. For a circular plume source of diameter D with a prescribed surface heat flux Q_p, the imposed buoyancy flux B_0 is given by

$$B_0 = \frac{g}{\theta_0} Q_p A = \frac{g}{\theta_0} Q_p \left(\frac{\pi D^2}{4} \right), \tag{7}$$

where g is gravitational acceleration, θ_0 is a reference potential temperature, and A is the source area. Equation (7) demonstrates that, for a fixed surface heat flux, the buoyancy flux scales quadratically with source diameter ($B_0 \propto D^2$), while changes in Q_p modulate the buoyancy forcing linearly.

Accordingly, sensitivity to plume diameter and surface heat flux cannot be considered independently: increasing the source diameter enhances the total buoyancy input primarily by increasing the integrated heat release area, whereas increasing Q_p intensifies buoyancy production per unit area. The plume responses reported in Table 6 therefore reflect how changes in the magnitude and spatial scale of buoyancy forcing interact with distinct ABL regimes to control vertical penetration, entrainment efficiency, and downstream transport.Specifically, as plume diameter increases, entrainment per unit plume mass decreases in the model, whereas as horizontal and/or vertical shear increases, entrainment per unit plume mass increases. The net effect on plume behavior depends on the combination of entrainment with plume buoyancy and ambient atmospheric conditions and must be assessed quantitatively.

Table 6 shows the plume-source sensitivity in terms of the ABL regimes identified in this study. Rather than treating plume diameter or buoyancy flux as universally controlling parameters, the table demonstrates that the plume response to source perturbations is strongly conditioned on the prevailing ABL regime. In nocturnal, shear-dominated conditions associated with a low-level jet, increases in source diameter or buoyancy primarily enhance near-source vigor, while vertical penetration remains limited by strong shear and stable stratification, resulting in efficient horizontal transport. During transitional regimes, plume response is most sensitive to buoyancy flux, as competition between shear and buoyancy allows partial penetration toward the inversion. In contrast, under convective mixed layer conditions, enhanced turbulence and entrainment rapidly dilute plume buoyancy, leading to weak sensitivity of plume height to source parameters and placing the dominant control on ABL depth. This regime-based perspective demonstrates that plume-source sensitivity cannot be interpreted independently of the evolving ABL state, reinforcing the central role of ABL regime characterization in wildfire plume modeling.

Table 6. Sensitivity of plume response to source parameters, conditioned on atmospheric boundary-layer (ABL) regimes identified in this study. Plume forcing is constrained by FRP; responses reflect regime-dependent filtering by ABL structure. ↑ denotes increase.

Source Perturbation	Nocturnal/Shear-Dominated (LLJ)	Transitional/Shear–Buoyancy	Convective Mixed Layer
Increase plume diameter (D)	• Total buoyancy ↑ ($\propto D^2$) • Vertical rise limited by inversion • Strong horizontal advection	• Enhanced entrainment • Partial penetration to inversion • Moderate downstream spread	• Rapid entrainment • Height capped by ABL depth • Increased lateral spreading
Increase surface heat flux (Q_p)	• Initial updraft ↑ • Shear suppresses vertical growth • Transport dominated by LLJ	• Stronger vertical velocities • Height sensitive to inversion strength • Regime-dependent response	• Diminishing height gain • Turbulence offsets buoyancy • Mixing dominates rise
Increase buoyancy flux (B_0)	• Near-source vigor ↑ • Limited vertical penetration • Efficient horizontal export	• Maximum sensitivity to B_0 • Possible partial lofting • Strong entrainment at cap	• Weak height sensitivity • Strong dilution • Height set by z_i
Extended forcing duration	• Sustained advection • Height unchanged	• Gradual plume adjustment • Height limited by regime	• Broader mixed layer • Vertical extent unchanged

6. Conclusions

The present work complements the CalFiDE field campaign by providing a high-resolution numerical modeling perspective on the role of ambient atmospheric conditions in governing wildfire smoke plume transport and mixing in complex terrain. Focusing on the Mosquito Fire, which was captured by MISR on 9 September at approximately 12 p.m. local time, the simulations resolve the evolving ABL in the Sierra Nevada region both prior to and during the satellite overpass. Using the WRF-ARW model driven by realistic boundary conditions from the HRRR system, the analysis demonstrates how the diurnal evolution of the terrain-modulated ABL through variations in boundary-layer depth, wind shear, and turbulence intensity directly influences plume rise, vertical mixing, and downstream transport. By explicitly resolving these processes using large-eddy simulation, the study highlights the critical role of complex terrain in shaping ABL structure and, consequently, buoyant plume behavior, providing a physically grounded interpretation of the MISR-observed plume characteristics and extending the observational insights obtained during the CalFiDE campaign.

The ABL simulations have been validated using 4 ASOS stations and the NOAA-MET Twin otter. With the low bias in 2 m temperature and humidity fields, as well as a good qualitative agreement with the upper-air wind speed and wind direction profiles, the WRF simulated meteorology is considered accurate for the plume simulations.

During the smoke-plume analysis period, the ABL transitions from a purely convective to a shear-buoyancy regime, which has an important effect on the horizontal transport scales of the fire plume. The horizontal transport scales of the plume are governed by wind shear, wind strength, and local atmospheric turbulence. The boundary layer depth, depth of the turbulent structures, and turbulence intensity in this layer influence the plume vertical transport scales.

During the nocturnal period, a weak low-level jet forms within the lowest few hundred meters, producing a near-surface horizontal wind maximum and strong shear confined near the surface. With the onset of daytime heating, vertical mixing weakens the nocturnal jet and redistributes momentum throughout the ABL, leading to a well-mixed horizontal wind profile by mid-afternoon. An elevated wind-speed maximum develops within the inversion layer, while winds above the inversion gradually transition toward geostrophic values.

Vertical velocities are weak and primarily mechanically driven during the stable nighttime period, with localized enhancements associated with near-surface shear and topographic effects. After sunrise, buoyancy-driven convection intensifies vertical motions, producing organized updraft–downdraft structures throughout the ABL. By midday, vertical transport dominates within the mixed layer, while vertical motions are strongly suppressed above the inversion.

During the nocturnal period, horizontal wind shear is strongly concentrated within a shallow layer near the surface as a weak low-level jet develops, with shear initially aligned with the inversion and progressively shifting downward overnight. Daytime surface heating weakens this near-surface shear and redistributes it throughout the ABL via turbulent mixing, while a pronounced shear layer persists within the capping inversion due to an elevated horizontal wind maximum.

Vertical shear is enhanced during the stable nighttime period and is closely tied to the formation of the low-level jet and terrain-induced flow acceleration, leading to mechanically generated turbulence near the surface. As convective conditions develop after sunrise, buoyancy-driven turbulence increases vertical momentum transport and reduces localized shear within the ABL, confining the strongest vertical shear to the inversion layer and the transition to the free troposphere.

Due to computational limitations, the domain for the plume numerical simulation is 5 km; hence, the plume can be tracked over a limited distance compared to the MISR observations, which capture a downwind plume extent estimated to represent about eight hours of smoke emissions. The vertical transport and the trends of the horizontal transport are in good qualitative agreement with the near-source MISR results.

Analysis of the temperature fields provides valuable insight into the influence of the plume on the micro-climate. The ABL is characterized by higher temperatures closer to the surface. As the high temperature plume interacts with the ambient temperature fields, the mixing and entrainment cause an increase in the ABL temperature and the mean temperature gradients. The mean temperature gradients result in the generation of additional turbulence fluctuations ([38]). The ABL turbulence is altered along the plume trajectory. As the scales of plume transport are on the order of a few kilometers, the influence of the plume on the micro-climate is significant.

This study advances the understanding of wildfire-ABL interactions through high-resolution large-eddy simulation, while explicitly anchoring plume forcing and vertical structure to satellite observations. Satellite-derived FRP from MODIS provides a physically based constraint on the magnitude of surface heat release, ensuring that the imposed plume buoyancy falls within a realistic range and avoids arbitrary tuning of source strength. Independent validation of plume rise and vertical structure using MISR stereo-retrieved plume heights further demonstrates that the simulated plume evolution is consistent with observed plume injection heights, vertical gradients, and downstream transport pathways.

The results highlight the critical role of realistic ABL conditions over complex topography in governing plume behavior. Plume rise and dispersion cannot be interpreted independently of the boundary-layer regime in which the plume develops; rather, ABL depth, stability, organized vertical motions, vertical and horizontal wind shear, and the distribution of turbulent kinetic energy collectively determine the efficiency of vertical penetration and horizontal transport. Although real wildfires involve additional complexities associated with fuel heterogeneity, fire growth, and time-varying heat release, the present results demonstrate that accurate characterization of the ambient ABL in real-time is a necessary prerequisite for physically meaningful wildfire plume modeling. By combining satellite-constrained plume forcing with independent validation of plume height and structure, this study provides a foundational contribution to the wildfire-ABL literature, isolating

and quantifying the coupled atmospheric and terrain controls on buoyant plume dynamics and laying the groundwork for more comprehensive, fully coupled fire-atmosphere modeling frameworks.

Future Work

Future extensions of this work will relax several idealizations adopted here in order to further bridge the gap between controlled numerical experiments and fully realistic wildfire conditions. In particular, subsequent studies will incorporate time-varying surface heat fluxes informed by evolving fire behavior and satellite-derived FRP, enabling the investigation of unsteady plume forcing and intermittent plume growth. Longer-duration plume simulations will be conducted to capture plume evolution beyond the first hour. Additional realism will be introduced through spatially heterogeneous heat-release patterns, multiple updraft cores, and explicit coupling to fuel properties and fire spread models. While these extensions are computationally demanding, the present study establishes a necessary foundation by demonstrating that accurate, plume-scale large-eddy simulation of the atmospheric boundary layer is a prerequisite for physically meaningful representation of wildfire plume dynamics under. complex terrain and strongly forced conditions.

Author Contributions: Conceptualization, K.B.; methodology K.B.; software, K.B. and S.R.B.; validation, S.R.B. and R.A.K.; formal analysis: K.B. and R.A.K.; investigation: K.B. and R.A.K.; data curation: K.B.; writing, K.B. and R.A.K.; Visualization K.B. All authors have read and agreed to the published version of the manuscript.

Funding: Funding for S.R.B. was provided by the NOAA cooperative agreement NA220AR4320151 for the Cooperative Institute for Earth System Research and Data Science (CIESRDS). The work of RK on this study was supported in part by the NASA ACMAP program under John Sullivan and the NASA MISR and Terra projects.

Data Availability Statement: The data will be available on request.

Acknowledgments: The authors thank Alan Brewer, Chemical Science Laboratory, NOAA for helping access and interpret the NOAA-MET Twin Otter flight observations used in this study. The statements, findings, conclusions, recommendations, and opinions expressed here are those of the authors and do not necessarily reflect the views of NOAA or the US Department of Commerce.

Conflicts of Interest: The authors declare no conflict of interest.

References

1. Murphy, P.; Mass, C. Weather Associated with Rapid-Growth California Wildfires. *Weather Forecast.* **2025**, *40*, 347–366. [CrossRef]
2. Sun, R.; Krueger, S.K.; Jenkins, M.A.; Zulauf, M.A.; Charney, J.J. The importance of fire-atmosphere coupling and boundary-layer turbulence to wildfire spread. *Int. J. Wildland Fire* **2009**, *18*, 50–60. [CrossRef]
3. Potter, B.E. Atmospheric interactions with wildland fire behaviour-I. Basic surface interactions, vertical profiles and synoptic structures. *Int. J. Wildland Fire* **2012**, *21*, 779–801. [CrossRef]
4. Coen, J.L.; Cameron, M.; Michalakes, J.; Patton, E.G.; Riggan, P.J.; Yedinak, K.M. WRF-Fire: Coupled weather-wildland fire modeling with the weather research and forecasting model. *J. Appl. Meteorol. Climatol.* **2013**, *52*, 16–38. [CrossRef]
5. Clements, C.B.; Lareau, N.P.; Seto, D.; Contezac, J.; Davis, B.; Teske, C.; Zajkowski, T.J.; Hudak, A.T.; Bright, B.C.; Dickinson, M.B.; et al. Fire weather conditions and fire–atmosphere interactions observed during low-intensity prescribed fires–RxCADRE 2012. *Int. J. Wildland Fire* **2015**, *25*, 90–101. [CrossRef]
6. Clements, C.B.; Kochanski, A.K.; Seto, D.; Davis, B.; Camacho, C.; Lareau, N.P.; Contezac, J.; Restaino, J.; Heilman, W.E.; Krueger, S.K.; et al. The FireFlux II experiment: A model-guided field experiment to improve understanding of fire–atmosphere interactions and fire spread. *Int. J. Wildland Fire* **2019**, *28*, 308–326. [CrossRef]
7. Heilman, W.E. Atmospheric turbulence and wildland fires: A review. *Int. J. Wildland Fire* **2023**, *32*, 476–495. [CrossRef]
8. Lareau, N.P. Plume Dynamics Drive Extreme Long-Range Spotting During California's Dixie Fire. *J. Geophys. Res. Atmos.* **2025**, *130*, e2024JD043167. [CrossRef]

9. Lecina-Diaz, J.; Alvarez, A.; Retana, J. Extreme Fire Severity Patterns in Topographic, Convective and Wind-Driven Historical Wildfires of Mediterranean Pine Forests. *PLoS ONE* **2014**, *9*, e85127. [CrossRef]
10. Dong, L.; Leung, L.R.; Qian, Y.; Zou, Y.; Song, F.; Chen, X. Meteorological environments associated with California wildfires and their potential roles in wildfire changes during 1984–2017. *J. Geophys. Res. Atmos.* **2021**, *126*, e2020JD033180. [CrossRef]
11. Abatzoglou, J.T.; Kolden, C.A.; Cullen, A.C.; Williams, A.P.; Balch, J.K.; Schoennagel, T. Climate change has increased the odds of extreme regional forest fire years globally. *Nat. Commun.* **2025**, *16*, 6390. [CrossRef] [PubMed]
12. Guirguis, K.; Hatchett, B.; Clemesha, R.; Aguilera, R.; Gershunov, A.; Campbell, I.; Cayan, D.; Merrifield, M. Compound atmospheric drivers of the catastrophic 2025 Los Angeles urban firestorm. *npj Nat. Hazards* **2025**, *2*, 103. [CrossRef]
13. Carroll, B.; Brewer, W.; Strobach, E.; Lareau, N.; Brown, S.; Valero, M.; Kochanski, A.; Clements, C.; Kahn, R.; Noyes, K.; et al. Measuring coupled fire-atmosphere dynamics: The California Fire Dynamics Experiment (CalFiDE). *Bull. Am. Meteorol. Soc.* **2024**, *105*, E690–E708. [CrossRef]
14. Noyes, K.; Kahn, R. Satellite multi-angle observations of wildfire smoke plumes during the CalFiDE field campaign: Aerosol plume heights, particle property evolution, and aging timescales. *J. Geophys. Res. Atmos.* **2024**, *129*, e2023JD039041. [CrossRef]
15. Strobach, E.J.; Carroll, B.J.; Baidar, S.; Zuraski, K. A Case Study Featuring the Time Evolution of a Fire-Induced Plume Jet Over the Rum Creek Fire: Mechanisms, Processes, and Dynamical Interplay. *J. Geophys. Res. Atmos.* **2024**, *129*, e2023JD040483. [CrossRef]
16. Kochanski, A.K.; Mallia, D.V.; Fearon, M.G.; Mandel, J.; Souri, A.H.; Brown, T. Modeling Wildfire Smoke Feedback Mechanisms Using a Coupled Fire-Atmosphere Model With a Radiatively Active Aerosol Scheme. *J. Geophys. Res. Atmos.* **2019**, *124*, 9099–9116. [CrossRef]
17. Menezes, I.; Lopes, D.; Fernandes, A.; Borrego, C.; Viegas, D.; Miranda, A. Atmospheric dynamics and fire-induced phenomena: Insights from a comprehensive analysis of the Sertã wildfire event. *Atmos. Res.* **2024**, *310*, 107649. [CrossRef]
18. Barjeste Vaezi, R.; Martin, M.R.; Hosseinpour, F. Impacts of wildfire smoke aerosols on radiation, clouds, precipitation, climate, and air quality. *Atmos. Environ. X* **2025**, *26*, 100322. [CrossRef]
19. Potter, B.E.; McEvoy, D. Weather Factors Associated with Extremely Large Fires and Fire Growth Days. *Earth Interact.* **2021**, *25*, 160–176. [CrossRef]
20. Peace, M.; Mattner, T.; Mills, G.; Kepert, J.; Mccaw, L. Fire-Modified Meteorology in a Coupled Fire–Atmosphere Model. *J. Appl. Meteorol. Climatol.* **2015**, *54*, 150113123251007. [CrossRef]
21. Fromm, M.; Servranckx, R.; Stocks, B.J.; Peterson, D.A. Understanding the critical elements of the pyrocumulonimbus storm sparked by high-intensity wildland fire. *Commun. Earth Environ.* **2022**, *3*, 243. [CrossRef]
22. Wasserman, T.N.; Mueller, S.E. Climate influences on future fire severity: A synthesis of climate-fire interactions and impacts on fire regimes, high-severity fire, and forests in the western United States. *Fire Ecol.* **2023**, *19*, 43. [CrossRef]
23. Driscoll, D.A.; Macdonald, K.J.; Gibson, R.K.; Doherty, T.S.; Nimmo, D.G.; Nolan, R.H.; Ritchie, E.G.; Williamson, G.J.; Heard, G.W.; Tasker, E.M.; et al. Biodiversity impacts of the 2019–2020 Australian megafires. *Nature* **2024**, *635*, 898–905. [CrossRef] [PubMed]
24. Cunningham, C.X.; Williamson, G.J.; Bowman, D.M. Increasing frequency and intensity of the most extreme wildfires on Earth. *Nat. Ecol. Evol.* **2024**, *8*, 1420–1425. [CrossRef]
25. Cannon, S.H.; DeGraff, J. The increasing wildfire and post-fire debris-flow threat in western USA, and implications for consequences of climate change. In *Landslides–Disaster Risk Reduction*; Springer: Berlin/Heidelberg, Germany, 2009; pp. 177–190.
26. Clarke, H.; Evans, J.P.; Pitman, A.J. Fire weather simulation skill by the Weather Research and Forecasting (WRF) model over south-east Australia from 1985 to 2009. *Int. J. Wildland Fire* **2013**, *22*, 739–756. [CrossRef]
27. Kumar, M.; Kosović, B.; Nayak, H.P.; Porter, W.C.; Randerson, J.T.; Banerjee, T. Evaluating the performance of WRF in simulating winds and surface meteorology during a Southern California wildfire event. *Front. Earth Sci.* **2024**, *11*, 1305124. [CrossRef]
28. De Wekker, S.F.; Kossmann, M.; Knievel, J.C.; Giovannini, L.; Gutmann, E.D.; Zardi, D. Meteorological applications benefiting from an improved understanding of atmospheric exchange processes over mountains. *Atmosphere* **2018**, *9*, 371. [CrossRef]
29. Andrews, P.L. BehavePlus fire modeling system: Past, present, and future. In Proceedings of the 7th Symposium on Fire and Forest Meteorology, Bar Harbor, ME, USA, 23–25 October 2007; American Meteorological Society: Boston, MA, USA, 2007; Volume 13, p. 2007.
30. Mölders, N. Suitability of the Weather Research and Forecasting (WRF) model to predict the June 2005 fire weather for Interior Alaska. *Weather Forecast.* **2008**, *23*, 953–973. [CrossRef]
31. Di Giuseppe, F.; Pappenberger, F.; Wetterhall, F.; Krzeminski, B.; Camia, A.; Libertá, G.; San Miguel, J. The potential predictability of fire danger provided by numerical weather prediction. *J. Appl. Meteorol. Climatol.* **2016**, *55*, 2469–2491. [CrossRef]
32. Shamsaei, K.; Juliano, T.W.; Roberts, M.; Ebrahimian, H.; Kosovic, B.; Lareau, N.P.; Taciroglu, E. Coupled fire-atmosphere simulation of the 2018 Camp Fire using WRF-Fire. *Int. J. Wildland Fire* **2023**, *32*, 195–221. [CrossRef]
33. Sullivan, A.L. Wildland surface fire spread modelling, 1990–2007. 1: Physical and quasi-physical models. *Int. J. Wildland Fire* **2009**, *18*, 349–368. [CrossRef]
34. Bowman, D.M.; Johnston, F.H. Wildfire smoke, fire management, and human health. *EcoHealth* **2005**, *2*, 76–80. [CrossRef]

35. Lareau, N.P.; Clements, C.B. The mean and turbulent properties of a wildfire convective plume. *J. Appl. Meteorol. Climatol.* **2017**, *56*, 2289–2299. [CrossRef]
36. Salesky, S.T.; Chamecki, M.; Bou-Zeid, E. On the nature of the transition between shear- and buoyancy-driven atmospheric boundary layers. *Bound.-Layer Meteorol.* **2017**, *163*, 41–68. [CrossRef]
37. Bhimireddy, S.R.; Bhaganagar, K. Implementing a new formulation in WRF-LES for Buoyant Plume Simulations: bPlume-WRF-LES model. *Mon. Weather Rev.* **2021**, *149*, 2299–2319. [CrossRef]
38. Chen, C.H.; Bhaganagar, K. Energetics of buoyancy-generated turbulent flows with active scalar: Pure buoyant plume. *J. Fluid Mech.* **2023**, *954*, A23. [CrossRef]
39. Chen, C.H.; Bhaganagar, K. New Findings in Vorticity Dynamics of Turbulent Buoyant Plumes. *Phys. Fluids* **2021**, *33*, 055112. [CrossRef]
40. Bhaganagar, K.; Bhimireddy, S.R. Numerical investigation of starting turbulent buoyant plumes released in neutral atmosphere. *J. Fluid Mech.* **2020**, *900*, A32. [CrossRef]
41. Bhaganagar, K.; Bhimireddy, S.R. Assessment of the plume dispersion due to chemical attack on April 4, 2017, in Syria. *Nat. Hazards* **2017**, *88*, 1893–1901. [CrossRef]
42. Bhimireddy, S.R.; Bhaganagar, K. Performance assessment of dynamic downscaling of WRF to simulate convective conditions during sagebrush phase 1 tracer experiments. *Atmosphere* **2018**, *9*, 505. [CrossRef]
43. Smagorinsky, J. General Circulation Experiments with the Primitive Equations. *Mon. Weather Rev.* **1963**, *91*, 99–164. [CrossRef]
44. Lilly, D.K. The representation of small-scale turbulence in numerical simulation experiments. In *NCAR Technical Report*; National Center for Atmospheric Research: Boulder, CO, USA, 1966.
45. Benjamin, S.G.; Weygandt, S.S.; Brown, J.M.; Hu, M.; Alexander, C.R.; Smirnova, T.G.; Olson, J.B.; James, E.P.; Dowell, D.C.; Grell, G.A.; et al. A North American hourly assimilation and model forecast cycle: The Rapid Refresh. *Mon. Weather Rev.* **2016**, *144*, 1669–1694. [CrossRef]
46. Mlawer, E.J.; Taubman, S.J.; Brown, P.D.; Iacono, M.J.; Clough, S.A. Radiative transfer for inhomogeneous atmospheres: RRTM, a validated correlated-k model for the longwave. *J. Geophys. Res. Atmos.* **1997**, *102*, 16663–16682. [CrossRef]
47. Dudhia, J. Numerical study of convection observed during the winter monsoon experiment using a mesoscale two-dimensional model. *J. Atmos. Sci.* **1989**, *46*, 3077–3107. [CrossRef]
48. Zhao, Q.; Black, T.L.; Baldwin, M.E. Implementation of the Cloud Prediction Scheme in the Eta Model at NCEP. *Weather Forecast.* **1997**, *12*, 697–712. [CrossRef]
49. Kain, J.S.; Fritsch, J.M. Convective parameterization for mesoscale models: The Kain-Fritsch scheme. In *The Representation of Cumulus Convection in Numerical Models*; Springer: Berlin/Heidelberg, Germany, 1993; pp. 165–170.
50. Hong, S.Y.; Noh, Y.; Dudhia, J. A new vertical diffusion package with an explicit treatment of entrainment processes. *Mon. Weather Rev.* **2006**, *134*, 2318–2341. [CrossRef]
51. Hu, X.M.; Nielsen-Gammon, J.W.; Zhang, F. Evaluation of three planetary boundary layer schemes in the WRF model. *J. Appl. Meteorol. Climatol.* **2010**, *49*, 1831–1844. [CrossRef]
52. Noh, Y.; Cheon, W.; Hong, S.; Raasch, S. Improvement of the K-profile model for the planetary boundary layer based on large eddy simulation data. *Bound. Layer Meteorol.* **2003**, *107*, 401–427. [CrossRef]
53. Chen, F.; Janjić, Z.; Mitchell, K. Impact of atmospheric surface-layer parameterizations in the new land-surface scheme of the NCEP mesoscale Eta model. *Bound.-Layer Meteorol.* **2003**, *85*, 391–421. [CrossRef]
54. Ek, M.; Mitchell, K.; Lin, Y.; Grunmann, P.; Rogers, E.; Gayno, G.; Koren, V.; Tarpley, J. Implementation of the upgraded Noah land-surface model in the NCEP operational mesoscale Eta model. *J. Geophys. Res.* **2003**, *108*, 8851.
55. NOAA National Weather Service. *Automated Surface Observing System (ASOS) User's Guide*; Technical Report; National Oceanic and Atmospheric Administration: Silver Spring, MD, USA, 1998; Updated periodically.
56. Jiménez, P.A.; Dudhia, J.; González-Rouco, J.F.; Montávez, J.; García-Bustamante, E.; Navarro, J.; Vilà-Guerau de Arellano, J.; Muñoz-Roldán, A. An evaluation of WRF's ability to reproduce the surface wind over complex terrain based on typical circulation patterns. *J. Geophys. Res. Atmos.* **2013**, *118*, 7651–7669. [CrossRef]
57. Solbakken, K.; Birkelund, Y.; Samuelsen, E.M. Evaluation of surface wind using WRF in complex terrain: Atmospheric input data and grid spacing. *Environ. Model. Softw.* **2021**, *145*, 105182. [CrossRef]
58. Monin, A.S.; Obukhov, A.M. Basic laws of turbulent mixing in the atmosphere near the ground. *Trudy Geofiz. Inst. Akad. Nauk SSSR* **1954**, *24*, 163–187.
59. Businger, J.A.; Wyngaard, J.C.; Izumi, Y.; Bradley, E.F. Flux–profile relationships in the atmospheric surface layer. *J. Atmos. Sci.* **1971**, *28*, 181–189. [CrossRef]
60. Stull, R.B. *An Introduction to Boundary Layer Meteorology*; Springer: Berlin/Heidelberg, Germany, 1988.
61. Wyngaard, J.C. *Turbulence in the Atmosphere*; Cambridge University Press: Cambridge, UK, 2010.
62. Deardorff, J.W. Convective velocity and temperature scales for the unstable planetary boundary layer. *J. Atmos. Sci.* **1970**, *27*, 1211–1213. [CrossRef]

63. Dosio, A.; Vilà-Guerau de Arellano, J. Statistics of absolute and relative dispersion in the atmospheric boundary layer. *Bound.-Layer Meteorol.* **2003**, *107*, 83–113.
64. Caputi, D.J.; Faloona, I.; Trousdell, J.; Smoot, J. ; Falk, N.; Conley, S. Residual layer ozone, mixing, and the nocturnal jet in California's San Joaquin Valley. *Atmos. Chem. Phys.* **2019**, *19*, 4721–4740. [CrossRef]
65. Parish, T.R. Forcing of the summertime low-level jet along the California coast. *J. Appl. Meteorol.* **2000**, *39*, 2421–2433. [CrossRef]
66. Whiteman, C.D.; Bian, X.; Zhong, S. Low-Level Jet Climatology from Enhanced Rawinsonde Observations at a Site in the Southern Great Plains. *J. Appl. Meteorol.* **1997**, *36*, 1363–1376. [CrossRef]
67. Weil, J.C.; Sullivan, P.P.; Patton, E.G.; Moeng, C.H. Statistical variability of dispersion in the convective boundary layer: Ensembles of simulations and observations. *Bound. Layer Meteorol.* **2012**, *145*, 185–210. [CrossRef]
68. Nelson, D.L.; Garay, M.J.; Kahn, R.A.; Dunst,B.A. Stereoscopic height and wind retrievals for aerosol plumes with the MISR Interactive eXplorer (MINX). *Remote Sens.* **2013**, *5*, 4593–4628. [CrossRef]
69. Junghenn Noyes, K.T.; Kahn, R.A.; Limbacher, J.A.; Li, Z.; Fenn, M.A.; Giles, D.M.; Hair, J.W.; Katich, J.M.; Moore, R.H.; Robinson, C.E.; et al. Wildfire Smoke Particle Properties and Evolution from Space-Based Multi-Angle Imaging II: The Williams Flats Fire during the FIREX-AQ Campaign. *Remote Sens.* **2020**, *12*, 3823. [CrossRef]

Disclaimer/Publisher's Note: The statements, opinions and data contained in all publications are solely those of the individual author(s) and contributor(s) and not of MDPI and/or the editor(s). MDPI and/or the editor(s) disclaim responsibility for any injury to people or property resulting from any ideas, methods, instructions or products referred to in the content.